Evidence for self-similar, triangular slip distributions on earthquakes: Implications for earthquake and fault mechanics.

Isabelle Manighetti, Michel Campillo, C. Sammis, P.M. Mai, G. King

Evidence for self-similar, triangular slip distributions on earthquakes: Implications for earthquake and fault mechanics

I. Manighetti,[1,2] M. Campillo,[3] C. Sammis,[1] P. M. Mai,[4] and G. King[5]

Received 12 May 2004; revised 26 January 2005; accepted 8 February 2005; published 13 May 2005.

[1] We characterize average slip distributions on earthquakes beyond their individual heterogeneity. For that, we analyze a large number of seismic slip distributions both measured at the surface after earthquakes (44 profiles) and derived from slip inversion models (76 models). Investigating the overall shape of these slip profiles, we find that they are roughly triangular both along strike and dip, and most of them (70–80%) are asymmetric. Long linear slopes and high slip gradients therefore are the key ingredients to describe earthquake slip profiles. The scaling relations between maximum displacement and length (or width) suggest furthermore that the triangular slip profiles are self-similar. Such slip patterns make earthquakes dominated by one major zone of maximum slip hence one major "asperity." Analyzing the position of hypocenters with respect to these "asperities," we find that earthquakes nucleate at a distance from them that averages 20–30% of their total length. Compiling observations on 56 earthquakes, we show that this distance (i.e., the asperity size) is structurally defined. We then compare the earthquake slip profiles to cumulative slip profiles measured on long-term faults of various ages and sizes and find that all profiles have a similar shape, triangular and asymmetric. Hence combining data for a large number of earthquakes leads to point out average, generic characteristics of the coseismic slip that are similar to those that emerge from the accumulation of events with time on a single fault. This suggests that these characteristics result from robust physical properties.

Citation: Manighetti, I., M. Campillo, C. Sammis, P. M. Mai, and G. King (2005), Evidence for self-similar, triangular slip distributions on earthquakes: Implications for earthquake and fault mechanics, *J. Geophys. Res.*, *110*, B05302, doi:10.1029/2004JB003174.

1. Introduction

[2] Our long-term objective is to understand further the processes of earthquakes and fault growth and how they are related. Faults grow through the addition of earthquakes (sometimes associated with creep). This process is not well understood, however, as it cannot be directly observed. Seismic (instantaneous) and cumulative (long term) slip distributions on faults represent two different stages of this process. Recognizing the similarities and differences between these two stages may help to understand better the process of fault growth, i.e., the way earthquakes follow in space and time to make a fault accumulate more slip and lengthen. Here, we address a series of simple questions: Do slip distributions on earthquake faults share any common characteristics? Do they resemble those on long-term faults? Do they provide information on earthquake and fault mechanics?

[3] Cracks in an elastic body have been widely used as a framework to characterize earthquakes with concepts such as stress drop and self-similarity. A first-order implication of this model is that its homogeneous conditions produce elliptical slip distributions on earthquake faults (although it is rarely mentioned that way). Introducing local dissipation at the crack tips make these slip distributions terminating with short tapers, however (so-called "tip tapers" [see *Scholz*, 2002]). In the last 20 years, many studies have combined different data sets acquired during or right after an earthquake to infer (through an inversion procedure) the slip distribution on the rupture plane [e.g., *Hartzell and Heaton*,1983; *Kikuchi and Fukao*, 1985; *Beroza and Spudich*, 1988; *Das and Kostrov*, 1990; *Cotton and Campillo*, 1995]. Hundreds of slip models have been produced (see supporting material[1] (files ES01–ES08)

[1]Department of Earth Sciences, University of Southern California, Los Angeles, California, USA.
[2]Now at Laboratoire de Géophysique Interne et Tectonophysique de Grenoble, Grenoble, France.
[3]Laboratoire de Géophysique Interne et Tectonophysique de Grenoble, Grenoble, France.
[4]Institute of Geophysics, ETH-Zurich, Zurich, Switzerland.
[5]Laboratoire de Tectonique, Institut de Physique du Globe de Paris, Paris, France.

0148-0227/05/2004JB003174$09.00

[1]Auxiliary material is available at ftp://ftp.agu.org/apend/jb/2004JB003174.

ES07 for references), each imaging the slip distribution on an earthquake fault. They revealed highly heterogeneous slip distributions, with patches of high slip separated by zones of low to zero slip. Yet, the studies that tried to compare these slip distributions were rare. *Somerville et al.* [1999] and *Mai and Beroza* [2002] did so, but they mainly focused on characterizing the earthquake slip complexity. The overall slip distribution patterns were not considered. In the mean time, surface measurements of seismic slip have accumulated. Many studies used these measurements to seek constraining specific scaling laws for earthquakes [e.g., *Wells and Coppersmith*, 1994; *Shaw and Scholz*, 2001, and references therein]. Studies devoted in the characterization of the slip distributions were rare. Using a few slip profiles, *Sieh* [1996] showed that the slip function could repeat similarly on some faults, but he did not examine these functions in further detail. *Hemphill-Haley and Wealdon* [1999] combined several slip profiles to develop a method for estimating the magnitude of prehistoric earthquakes, but they did not consider their overall shapes either. *Ward* [1997] did pay attention to shape but on the basis of one slip profile only. *Zhang et al.* [1999] analyzed several seismic slip profiles, but they only looked at their termination.

[4] Hence the questions related to the average shape of earthquake slip distributions are still opened. The available amount of data is now large enough to address them. Our approach emphasizes observations. Because earthquake studies lie at the boundary between seismology and tectonics, we combine observations and visions from these two domains. Our aim is to characterize average slip distributions on earthquakes beyond their individual heterogeneity. We use two types of data. First, we compiled (from literature) a large number of slip measurements performed at the surface after earthquakes. Some of these measurements are dense enough to show how slip varies along the whole rupture length. Some others were only done on specific sections of the ruptures (commonly, along major segments within ruptures). Some only consist of maximum displacement-length data. Taken together, however, these measurements allow distribution of surface slip along faults to be examined. Second, to know how total slip varies on entire fault planes, we analyze the slip distribution for 76 slip inversion models whose data have been compiled by P. M. Mai (2004, http://www.seismo.ethz.ch/srcmod). The profiles of maximum and mean slip that we extract from these models allow total slip variations along both fault strike and dip to be studied. We follow the general idea that analyzing many earthquakes together provides a way of smoothing their individual peculiarities (such as specific slip complexities), so that common, general properties, if any, may emerge. With this idea in mind, we successively analyze the overall shape of the slip profiles on earthquake faults, the position of hypocenters with respect to these slip distribution patterns, and the displacement length and width scaling relations for the available earthquakes. In each case, we find some general properties. Another idea is that cumulative slip distributions on long-term faults and systems, which result from the addition of a large number of earthquakes, give an over time-averaged image of earthquakes. Hence general properties of slip distributions should emerge in these cumulative slip distributions as well. We therefore compare our observations on earthquakes to those performed on cumulative faults and systems of various sizes and ages (10^4–10^6 years). This points out similar general properties. We end up discussing the implications of our results for earthquake and fault mechanics.

2. Data Sets

2.1. Surface Measurements of Seismic Slip

[5] From literature, we digitized 23 complete surface slip profiles (i.e., measured along whole length of earthquake rupture) and 20 partial profiles measured along segments within ruptures (Table 1). The retrieved data points have different spacing and precision, depending both on the original spacing and precision of the measurements and on the digitizing process. The corresponding earthquakes are spread worldwide and show various focal mechanisms and magnitudes (6.2–8.3, Table 1). We compiled most of the literature on these earthquakes and compared the various data acquired for each of them. In a few cases (indicated in Table 1), the surface rupture traces were found to extend slightly beyond the length (L_{meas}) along which slip had been measured (because slip at rupture tips is small and difficult to measure). In those cases, we added a point of zero slip to the available slip profiles where the ruptures were observed to actually end (see ES01 for details). The resulting rupture length is called L_{obs} (Table 1).

[6] While many earthquakes break the surface, most of them have no measured slip profile. At best, only their length and maximum slip have been measured. ES02 lists the earthquakes for which we found such measurements.

2.2. Two-Dimensional Earthquake Slip Inversion Models

2.2.1. Slip Models Deduced From Near-Field Data

[7] We use 76 published finite source rupture models that have been compiled by P. M. Mai (2004, http://www.seismo.ethz.ch/srcmod) (Table 2). The large majority are near-field inversion models. They image the overall slip distribution on 43 earthquake fault planes. These earthquakes are distributed worldwide and have various focal mechanisms (mostly strike slip, 45%; mostly dip slip, 55%), and magnitudes (M_w 5.5–8.0).

[8] The slip models were obtained using different data sources (geodetic, strong motion, teleseismic, local P waves, interferometric synthetic aperture radar, or, in best cases, a combination of two or more), inversion techniques, crustal models, methods to stabilize the inversion, and spatial sampling (see *Mai and Beroza* [2002] for details). They are therefore all quite different, and their relative "accuracy" is difficult to estimate. We consequently compare them using only their most basic attributes, i.e., data sources (number, location, quality, nature; Table 2, "data" values), their agreement with complementary observations (surface rupture geometry, distribution of immediate, on-fault aftershocks, etc; see ES01), their agreement with other models generated for the same earthquakes. The models that we eventually regard as being "best constrained" from these considerations are indicated in Table 2.

[9] In order to facilitate their comparison, the models were bilinearly interpolated onto 1×1 km grid spacing, so that large differences in spatial sampling could be smoothed

Table 1. Surface Data With Measured Slip Profile[a]

Earthquake	Event	Comments	Date	Kin	Mag	Main References	D_{max}	L_{meas}	L_{obs}
Entire Ruptures									
AL-Denali	S08		11/3/02	SS	7.9	*Eberhart-Philipps et al.* [2003]	9	340	340
AS-Kunlun	S27		11/14/01	SS	8.1	*Lin et al.* [2002]	16.3	400	400
AS-Manyi	S35		11/8/97	SS	7.6	*Peltzer et al.* [1999]	7	170	170
BR-Borah Peak	S03		10/28/83	N + SS	7.3	*Crone and Machette* [1984]	2.7	34	34
BR-Dixie Valley	S44		12/16/54	N	6.8	*Caskey and Wesnousky* [1997]	2.6	46	46
BR-Hebgen Lake	S19		8/17/59	N	7.5	*Zhang et al.* [1999]	5.6	26	26
BR-Pleasant Valley	S45		10/3/15	N + SS	7.7	*Zhang et al.* [1999]	5.8	60	60
IR-Fandoqa	S13		3/14/98	SS + N	6.6	*Berberian et al.* [2001]	3	25	25
IV-Borrego Mountain	S04		4/9/68	SS	6.6	*Wells and Coppersmith* [1994]	0.38	32	32
IV-Imperial Valley	S23		10/15/79	SS	6.6	*Sharp* [1982]	0.75	32	32
IV-Superstition Hill	S47		11/24/87	SS	6.6	*Sharp et al.* [1989]	0.52	25	25
L-Hector Mine	S22		10/16/99	SS	7.1	*Jonsson et al.* [2002]	6.4	60	60
L-Landers[b]	S33		6/28/92	SS	7.3	*Hernandez et al.* [1999] and *Sieh et al.* [1993]	6.7	71	85
PH-Luzon	S34		7/16/90	SS	7.7	*Velasco et al.* [1996]	6.2	130	130
SA-Fort Tejon	S14		1857	SS	7.8	*Hemphill-Haley and Weldon* [1999]	9.5	330	330
SA-San Francisco	S38		1906	SS	8.3	*Thatcher et al.* [1997]	8.6	480	480
TA-Chi Chi[b]	S05	DS motion	9/21/99	R + SS	7.7	*Dominguez et al.* [2003]	7.4	65	80
TA-Chi Chi	S06	SS motion	9/21/99	R + SS	7.7	*Dominguez et al.* [2003]	8.4	65	80
TU-Anatol Sequence	S01		1939–1967	SS		*Barka* [1996]	7.5	840	840
TU-Bolu Gerede	S02		2/1/44	SS	7.3	*Barka* [1996]	3.5	180	180
TU-Duzce	S46		11/12/99	SS	7.2	*Akyuz et al.* [2002]	4.8	40	40
TU-Erzincan	S10		12/26/39	SS	7.9	*Barka* [1996]	7.5	360	360
TU-Mudurnu	S36		7/22/67	SS	7.1	*Barka* [1996]	2	80	80
TU-Tosya	S41		11/26/43	SS	7.3	*Barka* [1996]	4.5	280	280
Segments									
AS-Fuyun[b]	S15	Main ST N	1931	SS	?	*Deng and Zang* [1984]	14.6	60	90
BR-Dixie Valley	S43	Main ST N	12/16/54	N	6.8	*Caskey and Wesnousky* [1997]	2.6	36	36
BR-Dixie Valley	S42	ST very N	12/16/54	N	6.8	*Caskey and Wesnousky* [1997]	2.45	24	24
BR-Dixie Valley	S48	ST S	12/16/54	N	6.8	*Caskey and Wesnousky* [1997]	0.63	7.5	7.5
BR-Fairview Peak	S12	Main ST S	12/16/54	N	7.1	*Caskey et al.* [1996]	3.8	19	19
BR-Fairview Peak	S11	GoldKing N	12/16/54	N	7.1	*Caskey et al.* [1996]	1	12.5	12.5
BR-Pleasant Valley	S37	Main ST S	10/3/15	N + SS	7.7	*Zhang et al.* [1999]	5.8	38	38
IR-Dasht e Bayaz[b]	S07	ST Nimbluk	8/31/68	SS	7.2	*Tchalenko and Berberian* [1975]	4.6	25	34
IV-Elmore Ranch	S09	ST ERF W	11/24/87	SS	6.2	*Hudnut et al.* [1989]	0.13	8	8
IV-Superstition Hill	S39	ST N	11/24/87	SS	6.6	*Sharp et al.* [1989]	0.52	15	15
IV-Superstition Hill	S40	ST S	11/24/87	SS	6.6	*Sharp et al.* [1989]	0.46	13.2	13.2
L-Hector Mine	S20	ST C-S	10/16/99	SS	7.1	*Jonsson et al.* [2002]	6.4	44	44
L-Hector Mine	S21	ST N	10/16/99	SS	7.1	*Jonsson et al.* [2002]	3.5	16	16
L-Landers	S28	ST CAMPROCK	6/28/92	SS	7.3	*Sieh* [1996]	1.2	7	7
L-Landers	S29	ST EMERSON	6/28/92	SS	7.3	*McGill and Rubin* [1999]	6	32	32
L-Landers	S30	ST ES2	6/28/92	SS	7.3	*Zachariasen and Sieh* [1995]	1.47	1.8	1.8
L-Landers	S31	ST ES3	6/28/92	SS	7.3	*Zachariasen and Sieh* [1995]	0.7	1.35	1.35
(L-Landers)	S32	ST Eureka	postslip	SS	7.3	*Peltzer et al.* [1994]	0.15	12.5	12.5
TU-Izmit[b]	S26	Main ST W (S2)	8/17/99	SS	7.4	*Michel and Avouac* [2002]	5.5	70	90
TU-Izmit + Duzce	S25	Main ST E (S3)	8/17and11/12/99	SS	7.4	*Hartleb et al.* [2002] and *Akyuz et al.* [2002]	4.8	68	68
TU-Izmit	S24	ST Sapanca	8/17/99	SS	7.4	*Barka et al.* [2002]	5	27	27

[a]Earthquakes with surface slip profiles analyzed, along entire rupture length and along segments within ruptures. Earthquakes are classified by regions (AL, Alaska; AS, Asia (China and Mongolia); BR, Basin and Range; IR, Iran; IV, Imperial Valley fault system; L, Landers fault system; PH, Philippines; SA, San Andreas fault system; TA, Taiwan; TU, Turkey). Chi-Chi has two profiles, for its lateral and dip-slip motions. Eureka (in parentheses) is only considered in scaling relations. ST, segment; DS, dip slip; SS, strike slip; N, S, W, E, C, north, south, west, east, and center, respectively; S2–S3 (Izmit-Duzce) defined in ES08. Kin, kinematics; SS, strike slip; N, normal; R, reverse. Mag, magnitude is that of corresponding earthquake. D_{max} and L_{meas} are maximum displacement (in m) and rupture length (in km) measured at surface, respectively; L_{obs} is total rupture length at surface, in km.

[b]Earthquakes with $L_{obs} > L_{mes}$ (see ES01).

(see *Mai and Beroza* [2002] for details). This interpolation process added some slip data to the original models. While this lets the overall slip distribution patterns unchanged, it modifies the values of maximum and mean displacements on the ruptures (dubbed D_{maxI} and D_{meanI}, respectively; Table 2). As these modifications are substantial (~10 and 27% for D_{max} and D_{mean}, respectively), we use the original data in our analysis of scaling relations (section 3.3). By contrast, we use the interpolated models in our analysis of slip profile shapes (section 3.1).

[10] The dimensions of the rupture planes used in the models (L_{model}, W_{model}) are generally chosen to be larger than the actual ones to ensure that the entire rupture is imaged. This makes most models having portions of low (often zero) or artifact slip at or close to their edges. Our first step was therefore to remove these artifacts and retrieve the actual length and width of the faults (L_{obs}, W_{obs}, Table 2). So far, this problem has been handled using statistical, systematic treatments. *Somerville et al.* [1999] systematically removed from all models that they analyzed any row or column whose mean slip was less than an arbitrary fraction of the mean slip for the entire model. *Mai and Beroza* [2000] instead used an autocorrelation method that led them to define an effective length at which zones of zero (or small)

Table 2. Models With Tabular Data Analyzed[a]

Earthquake	Event	Date	Kin	Mag	References	Data	L_{model}	L_{obs}	W_{model}	W_{obs}	D_{max}	D_{maxI}	D_{mean}	D_{meanI}	H
Antarctic-main[b]	59	3/25/98	SS	7.93	*Antolik et al.* [2000]	T	300	280	29	15	35.2	39.5	3	4.4	12
Antarctic-second[b]	60	3/25/98	N	6.2	*Antolik et al.* [2000]	T	70	70	27.2	15	21.1	22.8	2.8	3.2	12
Borah Peak[b,c]	16	10/28/83	N-LL	7.3	*Mendoza and Hartzell* [1988]	T	52	52	26	26	1.47	1.56	0.36	0.44	20
Central Chile[d,e]	20	3/3/85	R	8	*Mendoza et al.* [1994]	LS + SM + T	255	255	165	130	3.3	3.84	0.79	1.05	40
Chi-Chi[b,c]	73	9/21/99	R-LL	7.68	*Chi et al.* [2001]	SM	112	90	45.5	37	24.3	28.9	2.42	4.62	16
Chi-Chi[b,c]	74	9/21/99	R-LL	7.66	*Johnson et al.* [2001]	G	104	73	29	29	11.2	14.4	3.35	4.78	
Chi-Chi[b,c,f]	75	9/21/99	R-LL	7.68	*Ma et al.* [2001]	G + SM + T	80	80	45	45	15.5	20.7	3.6	5.72	17.6
Chi-Ch[c,d]	76	9/21/99	R-LL	7.62	*Zhang et al.* [2003]	SM	78	60	39	39	8.8	8.8	3	2.8	14
Chi-Chi[b,c,e]	77	9/21/99	R-LL	7.72	*Wu et al.* [2001]	G + SM	85	85	49	49	25.2	25.2	3.06	3.06	7.5
Chi-Chi[c,d]	78	9/21/99	R-LL	7.74	*Zeng and Anderson* [2000]	HF	84	84	42	42	4.59	6.71	0.64	2.96	14.5
Colima-Jalisco[b,e]	53	10/9/95	R	8	*Mendoza and Hartzell* [1999]	T	200	175	100	75	4.77	5.3	1.18	1.32	57.3
Coyote Valley	10	8/6/79	SS	5.69	*Liu and Helmberger* [1983]	SM	10	7	10	7	1.2	1.25	0.26	0.3	8
Duzce[b,c,e]	83	11/12/99	SS	7.21	*Delouis et al.* [2001]	R + T + Su	60	45	30	30	8	10.9	1.12	2.15	12.5
Duzce[b,c] (in event 70)	85	11/12/99	SS	7.1	*Delouis et al.* [2002]	G + R + SM + Su + T	65	60	22.5	22.5	6.8	8.8	1.27	2.16	13
Elmore Ranch[b,c]	28	11/24/87	SS	6.25	*Larsen et al.* [1992]	G	26	26	10	10	2.71	2.9	0.88	1.03	
Gifuken-Chubu[d]	03	9/9/69	SS	6.41	*Takeo* [1990]	SM	19	19	10	10	1.7	1.87	0.68	0.75	1.4
Hector Mine[b,c,f]	80	10/16/99	SS	7.22	*Ji et al.* [2002]	G + SM + Su + T	54	54	16	16	8.2	8.9	2.35	2.35	14.8
Hector Mine[c,d]	81	10/16/99	SS	7.22	*Kavarina et al.* [2002]	G + LS + R + Su + T	68	50	24	17	6.34	6.81	1.37	1.76	6
Hector Mine[b,c]	82	10/16/99	SS	7.16	*Salichon et al.* [2003]	G + R + T + Su	54	54	18	18	9.46	10.1	1.81	1.99	7.5
Huyga Nada 1[b]	54	10/19/96	R	6.8	*Yagi et al.* [1999]	G + SM	32	18	32	26	2.92	2.95	0.54	0.49	15
Huyga Nada 2[b]	55	12/2/96	R	6.7	*Yagi et al.* [1999]	G + SM	29	18	29	20	1.65	1.67	0.42	0.38	21
Imperial Valley[c,g]	11	10/15/79	SS	6.53	*Archuleta* [1984]	SM	35	35	13	10	1.78	1.75	0.46	0.47	8.5
Imperial Valley[b,c,e]	12	10/15/79	SS	6.62	*Hartzell and Heaton* [1983]	SM + T	42	42	10.5	10.5	1.8	2.05	0.59	0.62	10
Imperial Valley[b,c]	13	10/15/79	SS	6.47	*Zeng and Anderson* [2000]	HF	42	37	9	9	2.21	2.15	0.27	0.3	8
Izmit-S1S2[c,d,e]	68	8/17/99	SS	7.61	*Bouchon et al.* [2002]	SM	135	130	20	20	8.07	7.67	3.3	3.03	17
Izmit-S1S2[c,g]	69	8/17/99	SS	7.53	*Feigl et al.* [2002]	G + R + Su	128	143	21	21	5.65	6.23	2.07		15
Izmit-S1S2[b,c,d,f]	70	8/17/99	SS	7.4	*Delouis et al.* [2002]	G + R + SM + Su + T	105	135	22.5	22.5	8	10			13
Izmit-S1S2[c]	71	8/17/99	SS	7.41	*Segiguchi and Iwata* [2002]	SM	141	140	23.3	23.3	7.17	7.8	1.35	1.9	16
Izmit-S1S2[c,g]	72	8/17/99	SS	7.38	*Yagi and Kikuchi* [2000]	SM + T	93.6	138	21.6	21.6	6.31	6.23	2.24	1.96	16
(Izmit + Duzce)[c]	69	8/17/99	SS	7.53	*Feigl et al.* [2002]	G + R + Su	165	180	21	21	5.65	6.23	1.8	1.75	15
(Izmit + Duzce)[c]	70	8/17/99	SS	7.57	*Delouis et al.* [2002]	G + R + SM + Su + T	172	200	22.5	22.5	8	10	1.85	2.64	13
Izu-Hanto-Oki[b]	05	5/9/74	SS	6.54	*Takeo* [1990]	SM	25	25	8	8	3	3.1	1.06	1.08	7.5
Izu-Hanto-Oki[g]	14	6/29/80	SS	6.55	*Takeo* [1988]	SM	19	19	11	11	2.7	2.92	1.06	1.1	7.5
Joshua Tree	36	4/23/92	SS	6.25	*Bennett et al.* [1995]	G	35	30	20	19	0.84	0.84	0.11	0.11	15
Joshua Tree[b]	37	4/23/92	SS	6.14	*Hough and Dreger* [1995]	T	22	15	20	15	2.05	2.05	0.12	0.12	12.5
Kanto[c,d]	01	1/9/23	R-RL	7.82	*Wald and Somerville* [1995]	G + T	130	130	70	50	5.2	5.46	1.81	1.8	14.6
Kitamino[b]	02	8/19/61	R	6.47	*Takeo* [1990]	SM	15	15	11	11	1.6	1.81	0.9	0.74	6
Kobe[b]	48	1/17/95	SS	6.86	*Ide et al.* [1996]	SM	50	50	19	19	2.8	1.79		0.61	14.5
Kobe[d,f]	49	1/17/95	SS	6.74	*Sekiguchi et al.* [1996]	SM	64	55	19	19	3.11	3.06	0.73	0.67	16.4
Kobe[d]	50	1/17/95	SS	6.91	*Yoshida et al.* [1996]	G + LS + T	60	60	17	17	3.3	2.74	0.68	0.89	17
Kobe[b,e]	51	1/17/95	SS	6.91	*Wald* [1996]	G + SM + T	60	60	16	16	2.42	3.74	0.78	0.73	15
Kobe[b]	52	1/17/95	SS	6.93	*Zeng and Anderson* [2000]	HF	60	60	19	19	3.7	3.45	0.65	0.72	16.5
Landers[b,c,e]	38	6/28/92	SS	7.19	*Cohee and Beroza* [1994]	LS	83	100	18	18	6.08	6.62	1.31	1.52	5
Landers[b,c,e]	39	6/28/92	SS	7.31	*Cotton and Campillo* [1995]	SM	80	100	15	15	6.07	6.32	2.16	2.12	6
Landers[c,d,f]	40	6/28/92	SS	7.31	*Hernandez et al.* [1999]	G + R + SM + T	80	100	15	15	6.7	7.51	1.95	1.68	6
Landers[c,d,e]	41	6/28/92	SS	7.28	*Wald and Heaton* [1994]	G + SM + Su + T	78	100	14	14	7.94	8.42	2.4	2.64	6
Landers[c]	42	6/28/92	SS	7.22	*Zeng and Anderson* [2000]	HF	77	100	14	14	6.77	6.46	1.89	1.89	6.8
Loma Prieta[b,c,e]	31	10/18/89	R-RL	6.89	*Beroza* [1991]	SM	40	40	14	14	5.87	5.66	1.31	1.42	18
Loma Prieta[c,e]	32	10/18/89	R-RL	6.95	*Steidl et al.* [1991]	SM	38	38	17	17	4.34	5.56	1.38	1.89	18
Loma Prieta[c,g]	33	10/18/89	R-RL	6.95	*Wald et al.* [1991]	SM + T	40	40	19	19	5.51	5.68	1.07	1.13	17.3

Table 2. (continued)

Earthquake	Event	Date	Kin	Mag	References	Data	L_{model}	L_{obs}	W_{model}	W_{obs}	D_{max}	D_{maxI}	D_{mean}	D_{meanI}	H
Loma Prieta[b,c]	34	10/18/89	R-RL	6.98	*Zeng and Anderson* [2000]	HF	40	35	18	13	8.92	8.69	1.8	1.86	17.5
Michoacan[g]	21	9/19/85	R	8.02	*Mendoza and Hartzell* [1988]	T	180	150	139	130	7.49	8.3	1.4	1.69	17
Morgan Hill[g]	17	4/24/84	SS	6.24	*Beroza and Spudich* [1988]	SM	30	25	10	10	2.31	2.32	0.26	0.37	7
Morgan Hill[g]	18	4/24/84	SS	6.13	*Hartzell and Heaton* [1986]	SM + T	27	27	12	12	0.79	0.94	0.16	0.23	8.5
Naganoken[g]	19	9/14/84	SS	6.27	*Takeo* [1990]	SM	12	12	9	9	2.2	2.96	1.01	1.12	1.5
Nahanni 1[b]	23	10/5/85	R	6.7	*Hartzell et al.* [1994]	T	40	37	17	12	3.83	4.55	0.53	1.05	8
Nahanni 2[b]	24	12/23/85	R	6.78	*Hartzell et al.* [1994]	SM + T	48	48	21	21	5.16	5.68	0.48	0.92	8
North Palm Spring[d]	25	7/8/86	R	6.11	*Hartzell* [1989]	SM + T	22	20	15.2	12	0.45	0.56	0.14	0.18	11
North Palm Spring[b]	26	7/8/86	R	6.07	*Mendoza and Hartzell* [1988]	SM + T	22	20	15.2	14	0.89	0.96	0.13	0.17	11
Northridge[d]	43	1/17/94	R	6.65	*Dreger* [1994]	T	23	20	27	27	3.31	3.31	0.52	0.52	21.5
Northridge[b,e]	44	1/17/94	R	6.66	*Hartzell et al.* [1996]	SM	19	19	25	25	2.39	2.51	0.66	0.74	17.5
Northridge	45	1/17/94	R	6.81	*Hudnut et al.* [1996]	G		19	19	25	25	2.81	2.81	1.04	0.97
Northridge[d]	46	1/17/94	R	6.7	*Wald et al.* [1996]	G + SM + T	18	16	24	21	3	3.16	0.98	1.13	17.5
Northridge[b]	47	1/17/94	R	6.65	*Zeng and Anderson* [2000]	HF	18	18	24	24	0.89	0.86	0.14	0.15	17.5
Oaxaca[b]	79	9/30/99	N	7.5	*Hernandez et al.* [2001]	SM	90	80	45	37		2.8		0.8	39.5
Oitaken Chubu[b]	07	4/21/75	SS	6.36	*Takeo* [1990]	SM	9	9	9	9	2.5	2.74	1.28	1.07	8.3
Peru 74[e,g]	06	10/3/74	R	7.96	*Hartzell and Langer* [1993]	T	251	251	168	168	4.83	5.66	0.85	1.42	15
Peru 96[b]	56	11/12/96	R	7.89	*Salichon et al.* [2003]	R + T	180	180	120	100	4.37	4.98	0.49	1.09	22
Peru 96	57	11/12/96	R	7.9	*Spence et al.* [1999]	T	300	220	120	120	3.25	3.53	0.77	0.93	21
Petatlan[b]	09	3/14/79	R	7.36	*Mendoza* [1995]	T	120	87	120	120	1.22	1.34	0.29	0.38	15
Playa Azul[b]	15	10/25/81	R	7.23	*Mendoza* [1993]	T	58	54	70	60	4.04	4.72	0.49	1.07	14
San Fernando[b,c]	04	2/9/71	R	6.73	*Heaton* [1982]	SM + Su + T	18	18	19	19	5	5	1.6	1.6	15.4
Sierra Madre[b]	35	6/28/91	R	5.53	*Wald* [1992]	SM + T	6	6	5	5	1.39	1.16	0.17	0.22	3.4
Superstition Hills[c]	29	11/24/87	SS	6.71	*Larsen et al.* [1992]	G	24	24	9	9	3.06	4.08	1.12	1.94	
Superstition Hills[b,c]	30	11/24/87	SS	6.51	*Wald et al.* [1990]	SM	19	19	12	12	4.3	4.5	0.83	0.96	9
Tabas[b,c]	08	9/16/78	R-RL	7.12	*Hartzell and Mendoza* [1991]	SM + T	95	95	45	45	1.44	1.64	0.34	0.39	10.5
Tottori[b]	84	10/6/00	SS	6.79	*Iwata et al.* [2000]	SM	34	33	17.6	17.6	4.03	4.65	0.9	1.23	11
Yamaguchi[d]	58	6/25/97	SS	5.78	*Ide* [1999]	SM	15	12	12	12	0.51	0.52	0.09	0.12	7.6
Zihuatanejo[d]	22	9/21/85	R	7.38	*Mendoza* [1993]	T	90	80	90	75	2.09	2.34	0.43	0.57	20

[a]Earthquake slip models with tabular data analyzed (from http://www.seismo.ethz.ch/srcmod). Earthquakes in parentheses are not included in analysis of slip profile shapes. Event 85 is eastern part of event 70 (S3; see ES08). All abbreviations are as before, plus L_{model}, L_{obs}, model-inferred and "observed" rupture length, respectively (in km); W_{model}, W_{obs}, model-inferred and "observed" rupture width, respectively (in km); D_{max}, D_{maxI}, original and interpolated values of maximum displacement, respectively (in m); D_{mean}, D_{meanI}: original and interpolated values of mean displacement, respectively (in m); H, hypocenter depth (in km). Explanations for L_{obs} (or W) different from L_{model} (or W) are given in ES01. Data entries synthesize the types of data used in models (T, teleseismic; LS, local seismic; SM, strong motions; G, geodetic data, HF, high frequencies only; R, radar; Su, surface measurements). When several models show similar "rating," that with triangular slip profile both along strike and dip is preferred. Models 85, 81, 50, 51, 33, and 46 are not "preferred" although they are based on more data types. Reasons are that 85 is derived from model 70 and is not the best constrained part of the whole model; 81 is based on too few near-field seismic data; 50 and 51 include poorly constrained geodetic data that alter the models; 33 uses poorly constrained teleseismic data that may perturb the solution; and 46 incorporates geodetic data that include significant postslip and consequently alter the model.

[b]Models with slip profiles triangular-shaped along strike and along dip.

[c]Earthquakes with surface data available.

[d]Models with slip profiles triangular-shaped along strike.

[e]Best constrained models.

[f]Better constrained models.

[g]Models with slip profiles triangular-shaped along dip.

Table 3. Other Models With No Tabular Data Available[a]

Earthquake	Date	Kin	Mag	References	L_{model}	L_{obs}	W_{model}	W_{obs}	D_{max}	D_{mean}	H
AL-Alaska[b]	10/23/02	1	6.7	Kikuchi Web site[c]	40	40	20	20			10
AL-Denali[b,d]	11/3/02	1	7.9	Kikuchi Web site	280	280	40	40	14	4.3	15
Aqaba[b]	11/22/95	1	7.3	Kikuchi Web site	50	50	20	20	2.1		10
AS-Kunlun[b,d]	11/14/01	1	8.1	Kikuchi Web site	358	358	40	40			20
Bhuj[b]	1/26/01	2	7.6	*Antolik and Dreger* [2003]	50	60	36	36	12.4	3	22
Biak[b]	2/17/96	2	8.2	*Henry and Das* [2002]	230	230	100	100	12	4	12
Carlsberg[b]	7/15/03	1	7.6	Kikuchi Web site	220	220	39	39	4		15
Fiji[b]	10/14/97	2	7.7	Kikuchi Web site	70	70	70	70			185
FIJI-Tonga	3/9/94	2	7.6	*McGuire et al.* [1997]	80	80	75	75	4		564
Flores Sea[b]	6/17/96	1	7.9	Kikuchi Web site	70	70	70	70			587
GR-Athens[b]	9/7/99	2	5.9	*Roumelioti et al.* [2003]	11	11	13	13	0.95	0.16	8
IR-Iran[b]	5/10/97	1	7.2	Kikuchi Web site	110	110	20	20			15
J-Hokkaido-Nansei[b]	7/12/93	2	7.8	*Mendoza and Fukuyama* [1996]	200	200	70	70	4		20
J-Hokkaido-Toho[b]	10/4/94	1	8.2	Kikuchi Web site	140	140	60	60			50
J-Kushiro-Oki[b]	1/15/93	2	7.5	Kikuchi Web site	50	50	60	60			100
J-Tokachi-Oki	9/26/03	2	7.9	Kikuchi Web site	90	90	70	70	5.5		25
Java[b]	6/2/94	2	7.8	*Abercrombie et al.* [2001]	160	150	70	120	2.5		16
Kamchatka[b]	1/1/96	1	6.6	*Zobin and Levina* [1998]	75	55	60	60	2		10
Kuril	12/5/97	2	7.8	*Zobin and Levina* [2001]	250	250	150	150	2.4		
Mindanao[b]	3/5/02	2	7.3	Kikuchi Web site	60	60	50	50			30
Mindoro[b]	11/15/94	1	7.2	Kikuchi Web site	70	70	24	24			15
New Ireland[b]	11/16/00	1	8.1	Kikuchi Web site	200	200	40	40			35
Petrolia[b]	1992	2	7	*Oglesby and Archuleta* [1997]	28	28	29	29	3		10
Russia[b]	6/28/02	2	7.3	Kikuchi Web site	70	70	50	50			565
Sakhalin[b]	5/27/95	1	7	Kikuchi Web site	44	44	20	20			12
Sanriku	12/28/94	2	7.7	*Tanioka et al.* [1996]	240	240			1.7		
Scotia Sea[b]	8/4/03	1	7.5	Kikuchi Web site	60	60	30	30	6.2	2.7	20
SoAm-Bolivia	6/9/94	2	8.2	*Ihmlé* [1998]	135	135	120	120	4.5		650
SoAm-North Chile[b]	7/30/95	2	8.3	Kikuchi Web site	238	238	102	102			25
SoAm-Peru[b]	6/23/01	2	8.2	Kikuchi Web site	270	270	177	177	4.5	2.8	30
TA-Taiwan[b]	3/31/02	2	7.1	Kikuchi Web site	80	80	60	60			25
USA-New Brunswick[b]	1/9/82	2	5.6	*Hartzell et al.* [1994]	5	5	4	4	0.6		8
USA-Ungava[b]	12/25/89	2	6	*Hartzell et al.* [1994]	13	11.5	4	4	2.2		2.5
Uttarkashi	10/19/91	2	6.8	*Cotton and Campillo* [1996]	48	48	36	36	1.5		12.5
Yonaguni-Jima[b]	12/18/01	1	7.3	Kikuchi Web site	30	30	20	20			10

[a]Other earthquake slip models considered (no tabular data available). Earthquake names, abbreviations, and units as before plus J, Japan; and SoAm, South America. For kinematics, 1, strike slip; 2, dip slip. Explanations for few (L_{obs}, W_{obs}) different from (L_{model}, W_{model}) are given in ES01.
[b]With a slip model analyzed.
[c]Kikuchi Web site http://wwweic.eri.u-tokyo.ac.jp/EIC/.
[d]With surface data available (Table 1).

slip are not contributing, even when localized between slip patches. While these methods are useful to identify the zones that underwent some slip during the earthquakes, they are not appropriate to depict the overall shape of the ruptures. To retrieve the actual dimensions of the ruptures, we instead follow an ''observational'' approach that favors a ''case by case'' treatment (see ES01 for details). First, we removed from the models all slip artifacts described by the authors of the models. Then, we compared each model to other observations and data acquired for the corresponding earthquake. A particular attention was paid on the observation of surface breaks, on the geometry of the surface rupture if any (as it allows identifying main segments), and on the distribution of on-fault aftershocks immediately following (by a few days at most) the main shock (as those roughly define the fault dimensions [e.g., *Stein and Thatcher*, 1981; *Pegler and Das*, 1996]). We also compared the different models proposed for a given earthquake and checked for major discrepancies from one to the other. This analysis confirmed that most fault geometries used in inversions overestimate the dimensions of the rupture planes (see ES01 and ES03). A few models, however (i.e., those for Izmit and Landers), underestimate these dimensions. In those cases, it is the length of the modeled ruptures that is shorter than that deduced from surface observation and distribution of immediate, on-fault aftershocks. We handled these cases by adding to the original slip profiles a point of zero slip located where further observations suggest the rupture to actually end. This makes L_{obs} ~20–30% longer than L_{model} for these two earthquakes.

2.2.2. Complementary "Teleseismic" Earthquake Slip Models

[11] We broadened our study by examining 29 additional published slip models (indicated in Table 3). As tabular data were not available for these models, we only could visually inspect them and compile their parameters from the literature. Most of them are built from teleseismic data and hence are quite poorly constrained. The corresponding earthquakes have various focal mechanisms (dip slip, 60%) and magnitudes (M_w 5.6–8.3).

3. Data Analysis

3.1. Characterizing the Overall Shape of the Earthquake Slip Distributions

[12] In order to compare the one-dimensional (1-D) slip profiles measured at surface (along-strike profiles) to the total 2-D slip distributions modeled on fault planes, we analyze the later by depicting how maximum and mean slip vary both

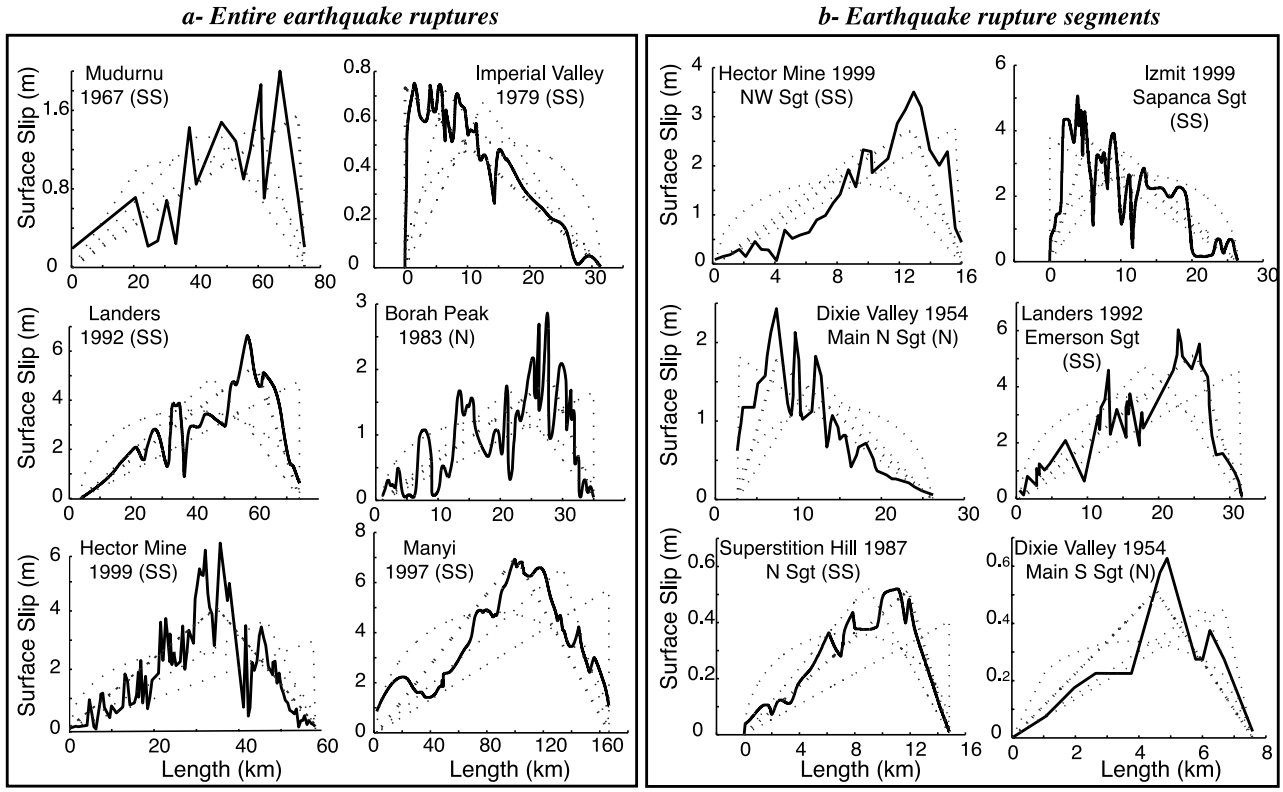

Figure 1. Examples of measured surface slip profiles. (a) Along entire rupture length. (b) Along rupture segments. All profiles are from Table 1. For each, the four attempts of shape correlation are shown in dotted lines, thicker for best fitting function. Sgt, segment; SS and N in parentheses, strike-slip and normal faults; N, S, W, and E, north, south, west, and east segments.

along the length (along-strike profiles) and along the width (along-dip profiles) of the faults. We therefore end up with a collection of one-dimensional profiles, each is given as D(x) (D is displacement or slip, both terms being used similarly; x is position along fault length or width). Hence all profiles are mathematically comparable and can be analyzed similarly, with a general procedure that we describe below.

[13] A visual inspection of the slip profiles having shown that most of them exhibit an overall triangular shape (see examples in Figure 1), we try to constrain this observation. We start by determining the X coordinate (normalized by X_{max}) of the center of gravity of each slip profile (X_{centr}). As the center of gravity of a profile is hardly sensitive to small-scale slip variability, it is a stable parameter that indicates the overall symmetry or asymmetry of the slip function. Any center of gravity located at $X_{centr} > 0.5$ (all X_{centr} are folded onto the [0.5–1] range on the basis of our choice to represent maximum slip always to the right) indicates a slip profile being asymmetric in shape, with an asymmetry more pronounced for higher X_{centr} values. If a slip profile really is triangular in shape, then its X_{centr} coordinate can be used to deduce the X_{apex} position of its apex (i.e., point of maximum slip; in any triangle, $X_{apex} = 3\ X_{centr} - 1$). Knowing this X_{apex} position, a correlation method is used to check how closely a triangle having its apex at X_{apex} approximates the actual slip profile. The coefficient of correlation is then compared to that that one would get from correlating the slip profile with an elliptical function (theoretical predicted pattern). Once the "best correlating" function is determined, the best fitting triangle or ellipse is calculated using a least squares method. In each population of slip profiles, the X_{centr} coordinates were found to more or less cover the full range of possible values ([0.5, 1]). This revealed that the profiles had various degrees of asymmetry. A few of them appeared more represented than others, however (larger number of X_{centr} around some specific values). We chose to use these few dominant degrees of asymmetry as a guide to discriminate the slip profiles otherwise mixed together in each population. From the few dominant X_{centr} values, we determined the corresponding X_{apex} coordinates. Only the few "reference triangles" having their apex at these specific X_{apex} values were then used for correlation to actual slip profiles. This defines a few groups of profiles approximated by the same reference triangle (or ellipse). In each group, profiles are then normalized by both their X_{max} (length or width) and D_{aver} (average slip for each profile). This makes them comparable one to the other regardless of slip variability and scale. The normalized profiles are finally superimposed (with some of them being flipped so that maximum slip is to the right in all cases), and their running average curve is calculated. The latter highlights the similar overall shape of the profiles.

3.1.1. Overall Shape of Seismic Slip Profiles Measured at Surface

3.1.1.1. Individual Earthquake Ruptures

[14] Figure 1a shows a few examples of slip profiles that were measured at the surface along the entire length of the earthquake ruptures indicated in the plots (see Table 1 for

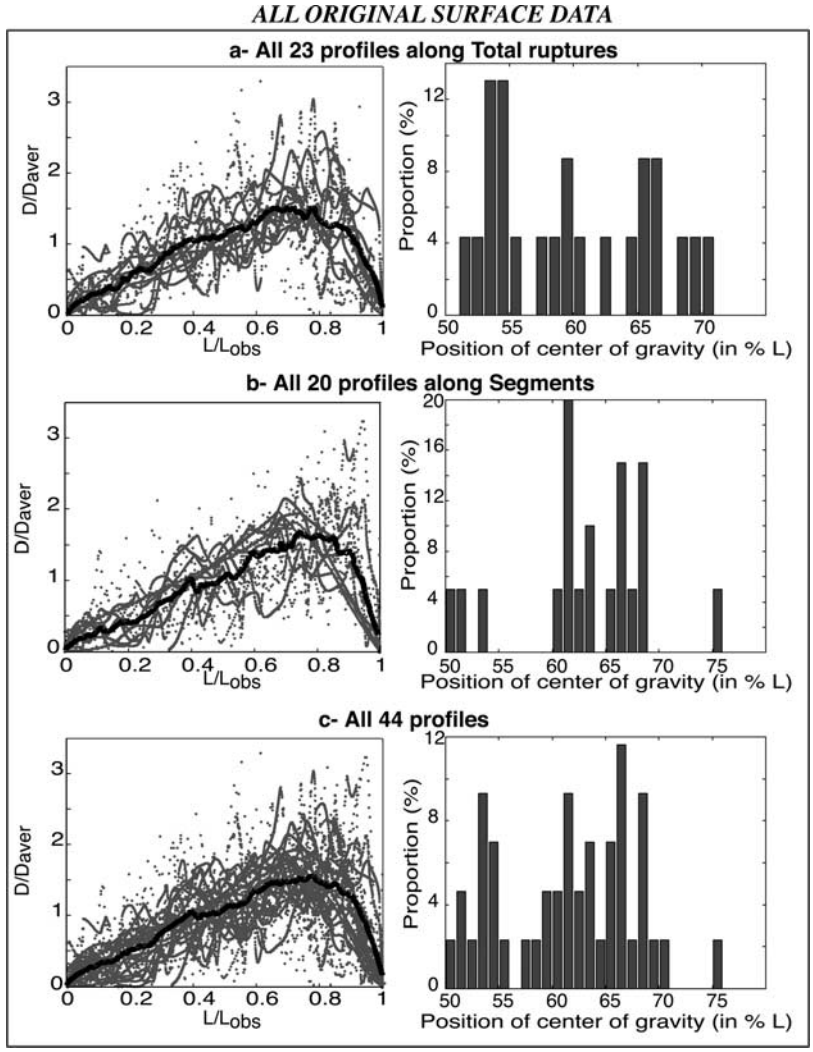

Figure 2. Overall shape of surface slip profiles. (a) All 23 surface slip profiles measured along entire rupture lengths (from Table 1, entire ruptures section). (b) All 20 surface slip profiles measured along rupture segments (from Table 1, segments section). (c) All 44 measured surface slip profiles (from Table 1; the plot includes one additional profile measured on the north Anatolian fault section broken in 1939–1967 sequence). (left) All profiles (dark gray) normalized by L_{obs} and D_{aver} (average slip for each profile) (with some of them being flipped so that maximum slip is to the right), with average curve calculated (black). (right) Histograms of positions of the centers of gravity of the profiles. Positions are reported to half fault length. The few $X_{centr} > 0.66$ result from having added a point of zero slip ahead of some original profiles.

details). Although these earthquakes differ in magnitude, focal mechanisms, location, and timing, the envelope of their surface slip profile looks similar overall, being roughly triangular. These triangular patterns have various degrees of asymmetry, however. Figure 2a (left) shows all 23 surface slip profiles from Table 1, normalized and superimposed as described before. Although all profiles show slip irregularities, their stacking defines an average curve that is roughly triangular and asymmetric. Figure 2a (right) is the histogram of X_{centr} for the 23 profiles. All X_{centr} are >0.51, with ~60% greater than 0.56. This shows that all profiles are asymmetric. This asymmetry is variable, however, so that Figure 2a (left) mixes together profiles being more or less skewed. Although the X_{centr} histogram suggests that a broad range of asymmetries may coexist in the original population, a few peaks are observed (grossly around 0.54, 0.59, and 0.66), which we use as a guide to distinguish the profiles otherwise mixed together in Figure 2a (left). Assuming that the profiles are triangular (Figures 1a and 2a, left), we hypothesize that the functions that best approximate them are triangles having their apex (X_{apex}) at ~60, 80, or 100% of the fault length. ES04a lists the coefficients of correlation ("Corr") obtained when comparing such reference triangles (dubbed TR60, TR80, and TR100) to the actual slip profiles. The coefficients of correlation obtained when an elliptical function (ELL) is used instead are added for comparison. The four correlating functions are represented in dotted lines for the few examples shown in Figure 1a, with the best fitting one in thicker line. ES04a shows that all but one slip profile are best approximated by a triangle, with

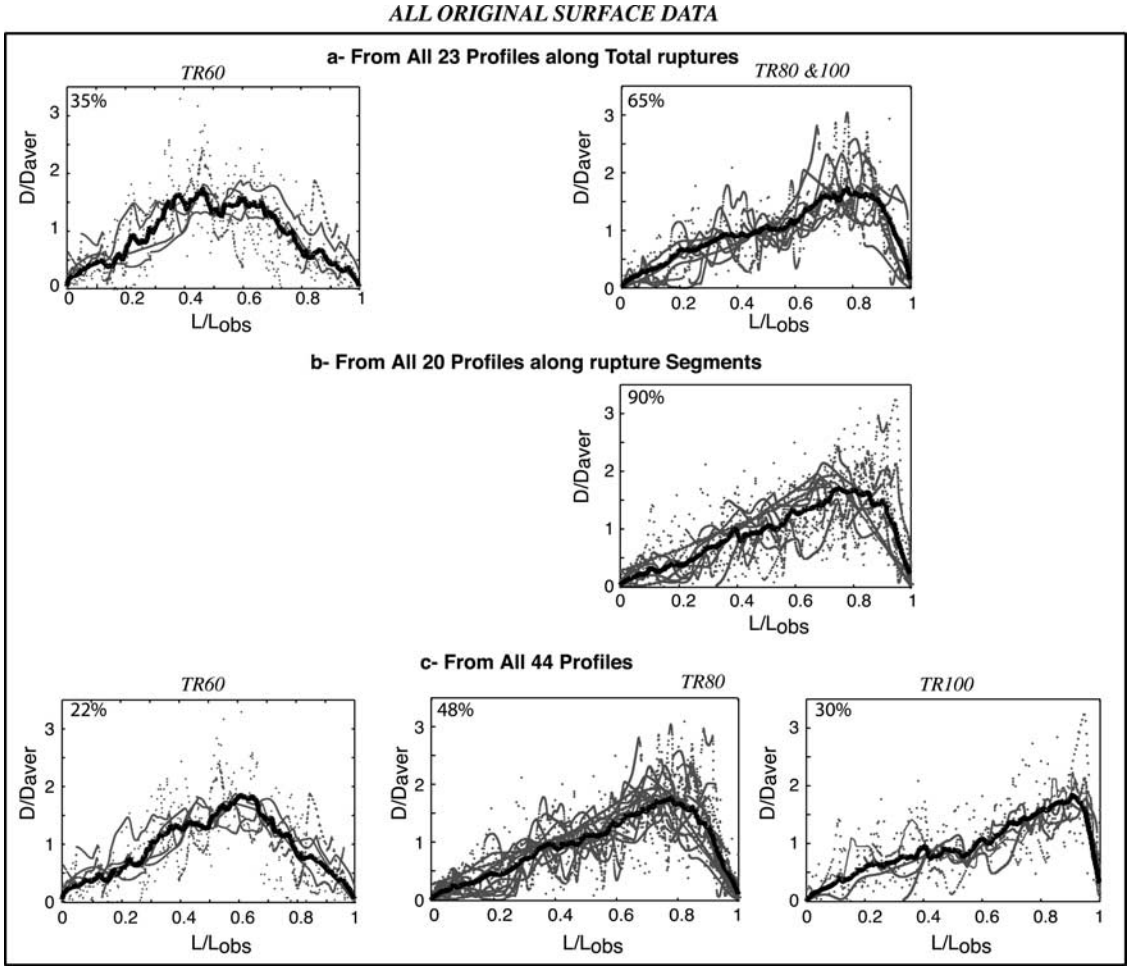

Figure 3. Dominant slip profile shapes identified from Figure 2. (a, b, c) Same populations of profiles as in Figure 2; each plot gathers profiles (percentages indicated) with same best correlating function (average curve in black). TR60, TR80, and TR100 indicate that corresponding reference triangles have their apex at 60, 80, and 100% of fault length, respectively.

Corr > 0.6 for all of them and >0.75 for ~70% of them. Twenty-six percent of the profiles are best approximated by a completely asymmetric triangle (X_{apex} = 1; Corr ~ 0.77), 39% are best approximated by a strongly asymmetric triangle (X_{apex} = 0.8; Corr ~ 0.84), and 30% are best approximated by a more symmetric triangle (X_{apex} = 0.6; Corr ~ 0.77). The slip profiles being best approximated by the same reference triangle are plotted together in Figure 3a (the TR80 and TR100 populations are considered together as data are too few to draw them separately), and their average curve is calculated. The latter highlights the overall similar shape of the profiles. For 65% of them, this shape is that of an asymmetric triangle, with slip decreasing roughly linearly from a maximum value at one rupture tip to zero at the other fault tip (Figure 3a, right). For the remaining 35%, the overall shape is that of a more symmetric triangle, with slip decreasing roughly linearly from a maximum value at about the fault center to zero at both rupture tips (Figure 3a, left). In both cases, the length of the linear sections is on the order of the total size of the event.

3.1.1.2. Segments Within Ruptures

[15] Most large irregularities in earthquake slip profiles are shown to correlate with fault segments within ruptures [e.g., *Segall and Pollard*, 1980; *Schwartz and Coppersmith*, 1984; *Machette et al.*, 1991; *Willemse*, 1997; *Hemphill-Haley and Weldon*, 1999]. Figure 1b shows a few examples of slip profiles measured at surface along such rupture segments. Again, the overall shape of these profiles looks similar, being roughly triangular and asymmetric. Figure 2b (left) shows all available segment profiles superimposed (Table 1). Although each profile is irregular in detail, the average curve calculated from them all again looks triangular and asymmetric. Eighty-five percent of the profiles have X_{centr} > 0.6 and hence are strongly asymmetric (Figure 2b, right). As the peaks in Figure 2b (right) are for X_{centr} values ~similar to those before, we correlate the segment slip profiles to the same TR60, TR80, and TR100 reference triangles (ES04b). We find that 30% of the profiles are best approximated by a completely asymmetric triangle (X_{apex} = 1; Corr ~ 0.67), 60% are best approximated by a strongly asymmetric triangle (X_{apex} = 0.8; Corr ~ 0.80), and 10% are best approximated by a roughly symmetric triangle (X_{apex} = 0.6; Corr ~ 0.88). Figure 3b shows all asymmetric segment profiles superimposed. It shows that slip along earthquake rupture segments generally decreases roughly linearly from a maximum value at one segment tip to zero or some low slip at the other

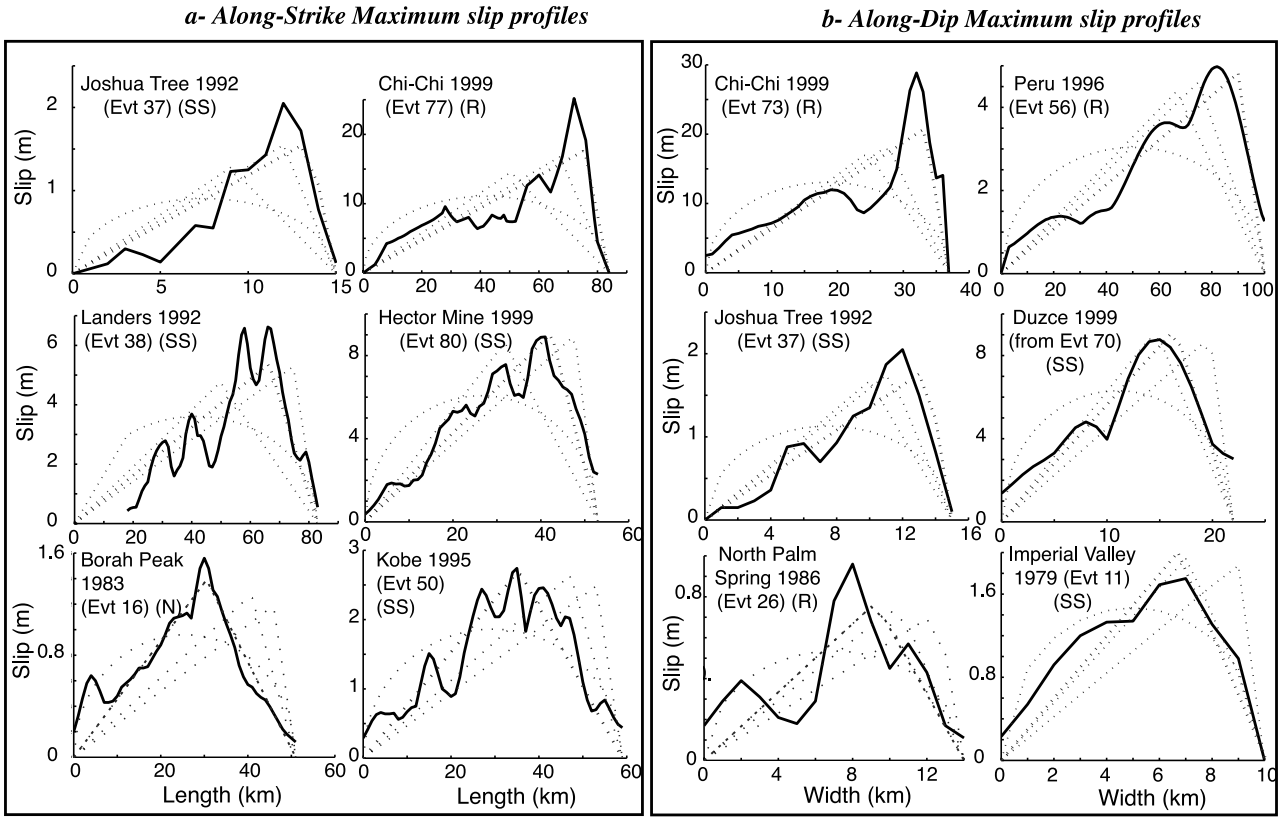

Figure 4. Examples of maximum slip profiles extracted from inversion models. (a) Along strike. (b) Along dip. All profiles are from Table 2. Caption is as for Figure 1 (R, reverse faults).

segment end. In all cases, the peak slip is found at the ''interior tip'' of the segments, while the linear sections are the ''exterior tips'' of the earthquake ruptures.

3.1.1.3. Synthesis

[16] Figure 2c (left) shows all analyzed surface slip profiles together (i.e., 44 profiles; details are given in Figure 2 caption), while Figure 3c distinguishes the three dominant patterns. A few profiles are quite symmetric (22%, Figure 3c, left), while the majority of them are strongly (48%, Figure 3c, middle) or completely asymmetric (30%, Figure 3c, right). These similar triangular shapes are found at all scales analyzed, from the smaller segment scale to the larger scale of individual ruptures, and for all focal mechanisms. This suggests that high slip gradients and long linear slopes (length similar to that of the event) are the key ingredients to describe surface slip distributions on earthquake faults.

3.1.2. Overall Shape of Slip Profiles Derived From Slip Inversion Models

[17] From the available slip models (Table 2), we extracted the profiles of maximum and mean slip both along the length (i.e., along strike) and along the width (i.e., along dip) of the fault planes. We ended with four populations of 77 slip profiles (76 + 1, as one model is split into the two distinct planes that it contains; see details in Table 2 and ES01). Since the rupture width is generally not well constrained, the along-strike profiles of mean slip give only a first-order view of the moment distribution on the fault plane. By contrast, zones of maximum slip are the best constrained on a modeled rupture plane. We therefore believe that profiles of maximum slip both along strike and dip give a satisfactory view of the overall slip distribution on the planes.

3.1.2.1. Overall Shape Of Along-Strike Slip Profiles

[18] Figure 4a shows a few examples of along strike profiles of maximum slip that we extracted from the earthquake models indicated. All profiles look triangular in shape and more or less asymmetric. Figure 5a shows all 77 along-strike slip profiles (maximum and mean slip on Figures 5a, left, and 5a, right, respectively). Although all profiles show slip irregularities, the stack draws a homogeneous average curve that looks roughly triangular and asymmetric overall. The histogram of X_{centr} (Figure 5a, middle) confirms that most profiles are asymmetric ($X_{centr} >$ 0.54 for ~70% of them) and can be compared to ''reference triangles'' having their apex at ~60, 80, or 90% of the fault length. The calculation (ES04c) indeed confirms that 23% of the profiles are well fitted by a roughly symmetric triangle (Corr $\sim$ 0.9), 27% are well fitted by a strongly asymmetric triangle (Corr $\sim$ 0.79), and 43% are well fitted by a completely asymmetric triangle (Corr $\sim$ 0.65) (Figure 6a). The remaining profiles (7%) are better approximated by an elliptical function (Corr $\sim$ 0.5).

[19] To further refine our observations, we now consider only the models for earthquakes with a magnitude >6.5, which are the best constrained. This new population includes 63 models over the initial 77. Figures 5b and 6b are done as before for this population. The results are the same: The stacked maximum and mean slip profiles draw a triangular and asymmetric average curve, while the same three dominant degrees of asymmetry are revealed. Figure 5c

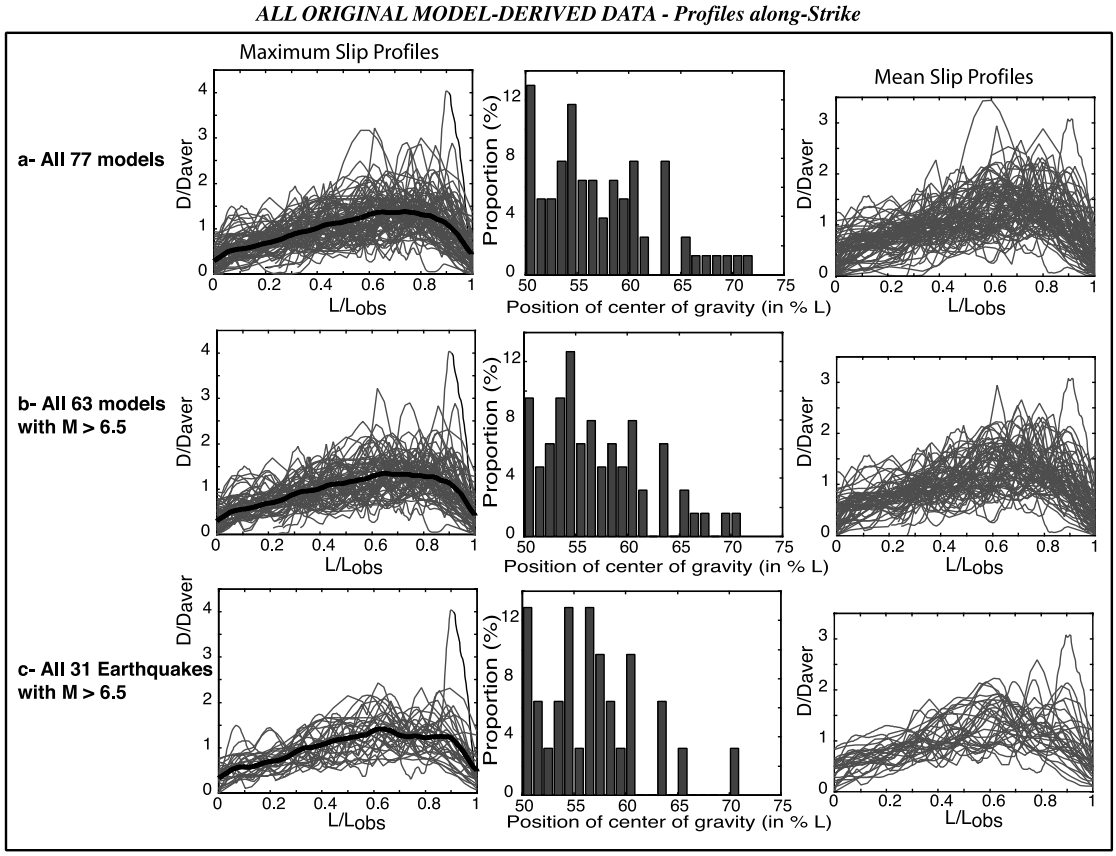

Figure 5. Overall shape of along-strike slip profiles extracted from inversion models (Table 2). (a) All 77 models. (b) All 63 models for earthquakes with M > 6.5. (c) All 31 "earthquakes" with M > 6.5 (i.e., one model only is kept per earthquake, chosen according to Table 2). (left) maximum slip profiles (gray) normalized (by L_{obs} and D_{aver}; D_{aver} is average slip for each profile) and superimposed as before. Average curve is black. Profiles are obtained by extracting the maximum slip value per column and plotting these values as a function of fault length. (middle) Histograms of positions of centers of gravity of maximum slip profiles. (right) Mean slip profiles normalized (by L_{obs} and D_{aver}) and superimposed. Profiles are obtained by calculating the mean slip value per column and plotting these values as a function of fault length. Mean slip therefore directly depends on W (poorly constrained), while maximum slip does not. The few slip profiles that do not end at x = 0 are those with $L_{obs} > L_{model}$. None of the average curves reaches zero at its tips because slip near fault edge is poorly constrained.

now shows the distribution of along-strike slip profiles for a population where only one model is kept per earthquake with magnitude >6.5. This population represents a total of 31 earthquakes. The maximum and mean slip profiles for these earthquake ruptures also are roughly triangular in shape, with most being completely (39%) or strongly asymmetric (26%) and the remaining quite symmetric (32%) (Figure 6c).

3.1.2.2. Overall Shape of the Along-Dip Slip Profiles

[20] We now consider the distributions of slip along the width of the fault planes. As the boundary conditions at the free surface and at the base of the seismogenic zone are different, one may expect the overall shape of the along-dip slip profiles to be different for ruptures at different depths. Yet, if such differences exist, the simple treatments that we apply to the profiles should make them clear.

[21] A few examples of along-dip (maximum) slip profiles are shown in Figure 4b. All show a triangular and more or less asymmetric overall shape. Figures 7a and 8a show the complete population of along-dip slip profiles (represented as before). The stacked profiles draw a homogeneous pattern, suggesting that the individual profiles are not significantly different in shape whether their maximum slip is close to surface or is at depth. Figure 9, on which profiles having their peak slip close to either the fault top or base are distinguished, confirms this point. All profiles have a similar shape, roughly triangular and asymmetric (note, however, that slip does not necessarily go down to zero at surface, while it does at depth). The X_{centr} histogram (Figure 7a, middle) suggests that most profiles can be correlated to reference triangles having their apex at ~66, 75, or 90% of the fault width. The calculation (ES04d) indeed confirms that 43% of the profiles resemble a completely asymmetric triangle (X_{apex} = 0.9, Figure 8a, right; Corr ~ 0.71), 27% resemble a strongly asymmetric triangle (X_{apex} = 0.75; Figure 8a, middle; Corr ~ 0.82), and 14% resemble a roughly symmetric triangle (X_{apex} = 0.66; Figure 8a, left; Corr ~ 0.85). The remaining profiles (15%) are best approximated by an elliptical function (Corr ~ 0.87). Figures 7b and 8b are done as before for the

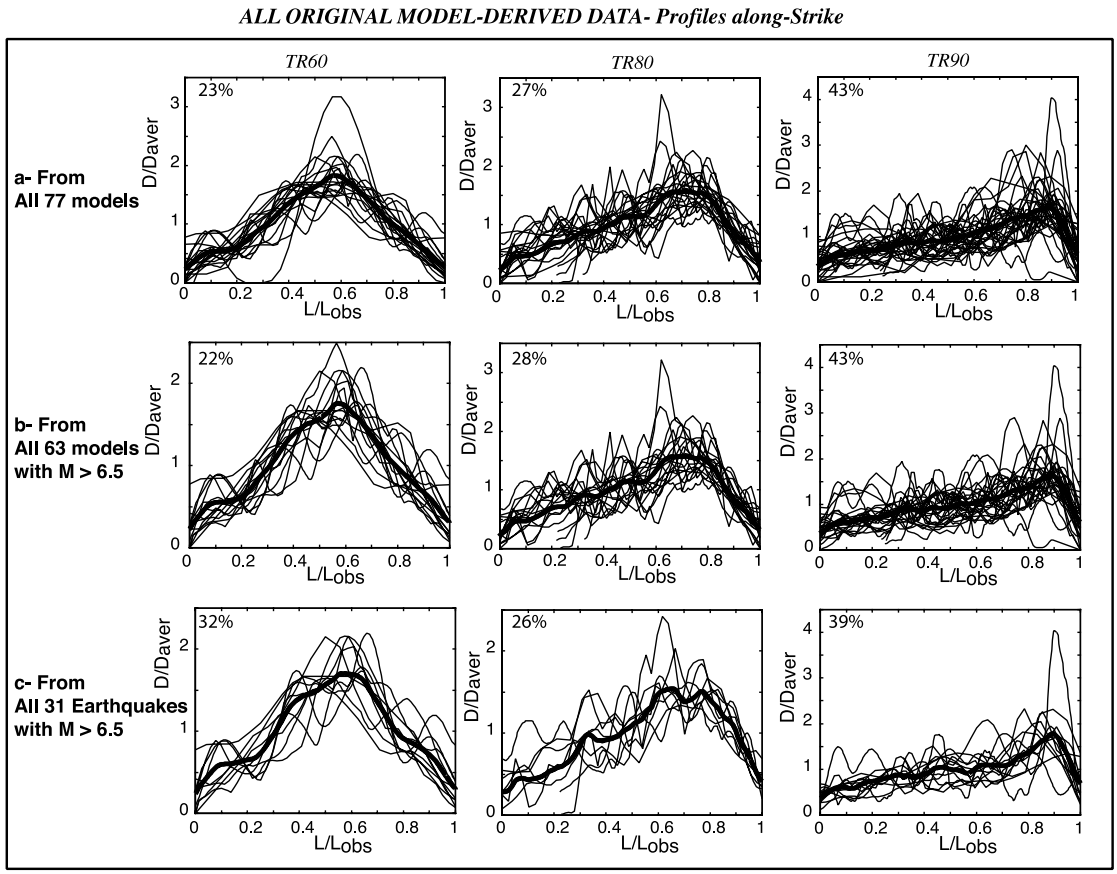

Figure 6. Dominant slip profile shapes identified from Figure 5 (maximum slip profiles only). (a, b, c) Same populations of profiles as in Figure 5. Each plot gathers profiles (percentages indicated) with same best correlating function (average curve black). TRX is as in Figure 3.

63 models performed for earthquakes with $M_w > 6.5$, while Figures 7c and 8c show the along-dip slip profiles for the population of 31 earthquakes with magnitude >6.5. In both cases, results are similar to those found before: Maximum and mean slip profiles are triangular in shape, and most of them are completely or strongly asymmetric.

3.1.2.3. Synthesis

[22] The above analysis shows that most studied earthquake faults have similar triangular-shaped slip profiles, both along strike and dip. Besides, most of these profiles (70–80%) are strongly asymmetric. Thus, on most earthquake ruptures, slip ramps up roughly linearly from both tips to a peak value (more or less rounded apex). That peak may be in the fault center but is more often off to the side. In the latter case, the taper to the end nearest to the peak is much steeper than the taper on the other side. That gentle linear taper is long, roughly on the entire length (and width) of the event. These results are found at all scales analyzed (see also ES05 where slip profiles are distinguished on the basis of earthquake magnitudes) and for all focal mechanisms. The visual inspection of the additional slip models that we found in the literature (Table 3) reveals that most of them show a roughly regular slip decrease both along strike and dip from a maximum value close to one fault edge to zero (or almost) at the other fault edge. The corresponding maximum slip profiles are therefore also expected to be roughly triangular in shape and asymmetric both along strike and dip. This suggests that our results can be generalized to most earthquake ruptures.

[23] That all faults analyzed have triangular-shaped slip profiles is confirmed by Figure 10 that shows that, for each population of profiles, D_{max} is about twice D_{aver}, as expected for triangular functions. Therefore, on average, slip distributions on earthquakes are far from being elliptical as it is implicitly predicted from the simple crack model. Besides, the observed triangular shapes reveal linear tapers that are at the scale of the event itself and hence much longer than the ''tip tapers'' supposed to accommodate the stress singularities at the very rupture ends [e.g., *Barenblatt*, 1962; *Ida*, 1972; *Scholz*, 2002]. Thus the process responsible for this major discrepancy with the crack model cannot be solely controlled by the stress singularity at the fault tips.

3.2. Analyzing the Position of Hypocenter With Respect to Slip Distribution Patterns

[24] Having shown that slip distributions on earthquake faults have a well-defined overall shape, we now investigate if any particular relation exists between the ''point'' of earthquake initiation (i.e., the hypocenter) and these shapes. We are aware that hypocenters may not represent the exact points of rupture nucleation or start of moment release [e.g., *Campillo and Archuleta*, 1993; *Abercrombie and Mori*, 1994; *Mori*, 1996; *Perfettini et al.*, 1999]. We nevertheless assume that published hypocenters reasonably indicate the

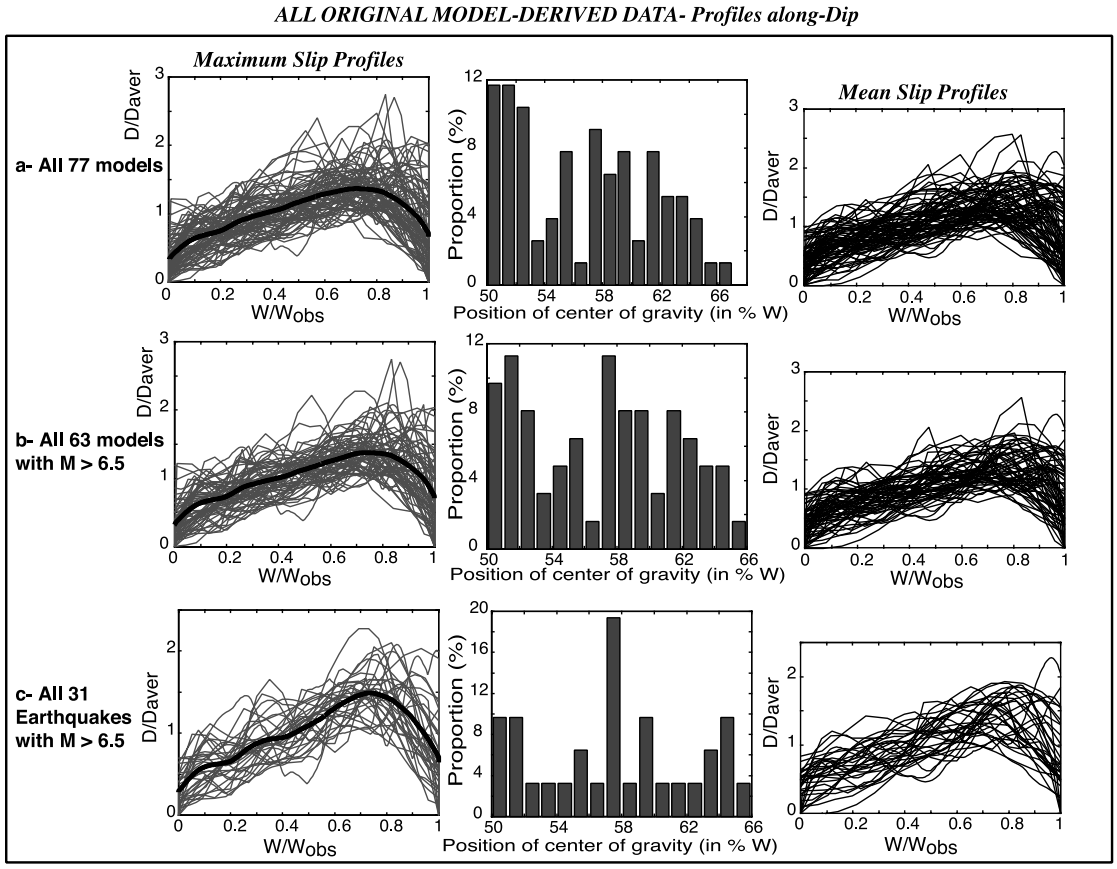

Figure 7. Overall shape of along-dip slip profiles extracted from inversion models (Table 2). (a) All 77 models. (b) All 63 models for earthquakes with M > 6.5. (c) All 31 earthquakes with M > 6.5 (i.e., one model only is kept per earthquake, chosen according to Table 2). Same as Figure 5, but with W replacing L. Profiles of maximum slip are obtained by extracting maximum slip value per line and plotting these values as a function of fault width. Profiles of mean slip are obtained by calculating the mean slip value per line and plotting these values as a function of fault width. Mean slip therefore depends on L, while maximum slip does not.

region where rupture initiated within the fault planes. Because of this difficulty, we have assigned to all hypocenter coordinates a large, 5 km uncertainty in both X and Z directions. Few studies (except *Somerville et al.* [1999] and *Mai et al.* [2005]) have been carried out to analyze the position of hypocenters within fault zones in a systematic way. As our goal is to analyze the positions of hypocenters with respect to the overall slip distributions, we use the (L_{obs}, W_{obs}) rupture plane dimensions.

3.2.1. Position of Hypocenters With Respect to Fault Plane Edges

[25] Figure 11a shows the position of hypocenters (from Table 2; averaged per earthquake) with respect to the edges of the rupture planes. The symbol surface is proportional to magnitude. Dip-slip and strike-slip (plus oblique) ruptures are in blue and red, respectively. Position along rupture length is analyzed with respect to closest lateral fault edge and hence along the fault half length. By contrast, position along rupture width is considered with respect to fault base and hence along the entire fault width. Figure 11a shows that hypocenters are quite evenly distributed along the width of the faults. A larger number is found, however, at 20 ± 10% of the fault width from its base, while only few hypocenters locate close to the fault top. Most large magnitude strike-slip earthquakes nucleate close to either the fault base or the half width, while most dip-slip earthquakes nucleate close to either the fault base or the top. These observations are similar to those made by *Somerville et al.* [1999] on a smaller data set. Together these show that while many earthquakes nucleate close to the base of the brittle crust [e.g., *Das and Scholz*, 1983; *Sibson*, 1984; *Choy and Dewey*, 1988; *Mendoza et al.*, 1994; *Boatwright and Cocco*, 1996; *Huc et al.*, 1998; *Chambon and Rudnicki*, 2001], many others do not and initiate at shallow depth. Most ruptures nucleating in the top half of the fault planes have their slip tapering downward (yellow circled symbols). Most ruptures nucleating in the bottom half of the planes have their slip tapering upward (green circled symbols).

[26] Figure 11b is similar to Figure 11a, but with symbol surfaces now proportional to D_{max}/L_{model} ratios (Figure 11b includes additional data from Table 3). These ratios give a first-order view of the amount of slip accumulated over the fault planes and an idea of the stress drop for the corresponding earthquakes (for a given range of W and in the hypothesis of elastic cracks). Figure 11b shows that the larger ratios (i.e., higher stress drops) are found for the ruptures nucleating close to the fault base. These are not necessarily the largest magnitude earthquakes. Largest events

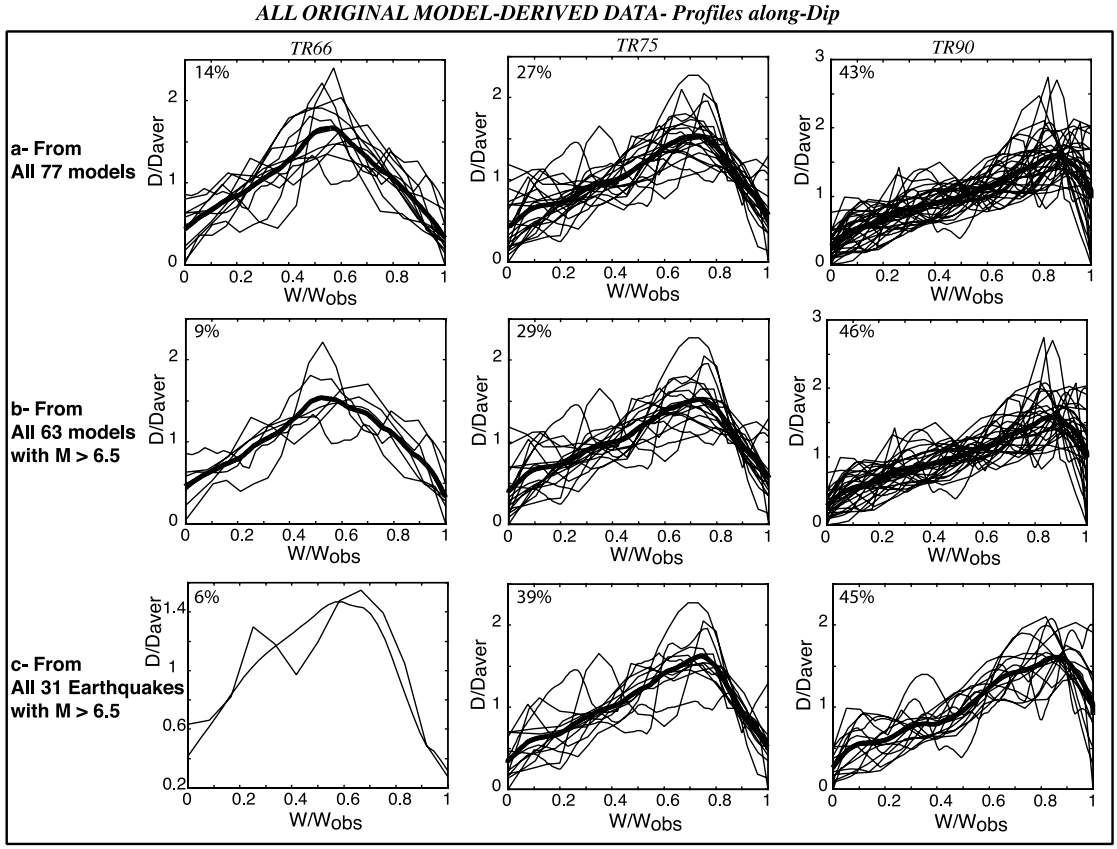

Figure 8. Dominant slip profile shapes identified from Figure 7 (maximum slip profiles only). (a, b, c) Same populations of profiles as in Figure 7. Each plot gathers profiles (percentages indicated) with same best correlating function (average curve in black). TRX as in Figure 3 (with L replaced by W).

actually seem to have the smallest ratios; that is, large earthquakes have smaller average stress drops than others.

3.2.2. Position of Hypocenters With Respect to Zone of Maximum Slip

[27] Zones of large slip (relative to the rest of the slip on the fault) on earthquake fault surfaces are usually defined as "asperities" [e.g., *Madariaga*, 1979; *Lay and Kanamori*, 1981; *Das and Kostrov*, 1983; *Mendoza*, 1993; *Ruff and Miller*, 1994; *Somerville et al.*, 1999; *Papageorgiou*, 2003; *Das*, 2003]. In section 5, we will discuss how these asperities relate to geological structures. The observation of overall triangular slip profiles on earthquake faults (both along strike and dip) make these profiles shaped by one single zone of maximum slip. Hence, while many events have slip profiles with several peaks [*Thatcher*, 1990; *Somerville et al.*, 1999], one is dominant (in terms of slip and moment) over the others. Here we analyze the position of hypocenters with respect to these major asperities (identified as the zones of maximum slip in the profiles) for the population of earthquakes that we found to have a triangular slip profile both along strike and dip. Figure 12a shows the hypocenter positions for data from Table 2 (averaged per earthquake, solid symbols) and Table 3 (open symbols). The X axis is the along-strike distance (HA_x) between an hypocenter and the apex (i.e., zone of maximum slip) of the reference triangle that best fits the along-strike maximum slip profile of its corresponding earthquake (for Table 2 data; otherwise, handmade measurements for Table 3

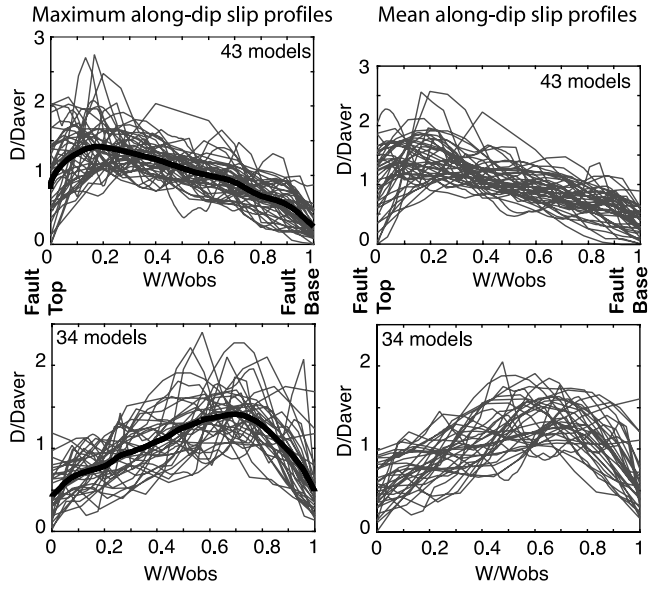

Figure 9. Influence of depth on overall shape of along-dip slip profiles. (left) Maximum and (right) mean slip profiles. (top) Profiles having their peak slip close to surface. (bottom) Profiles having their peak slip at depth. Otherwise as previous figures.

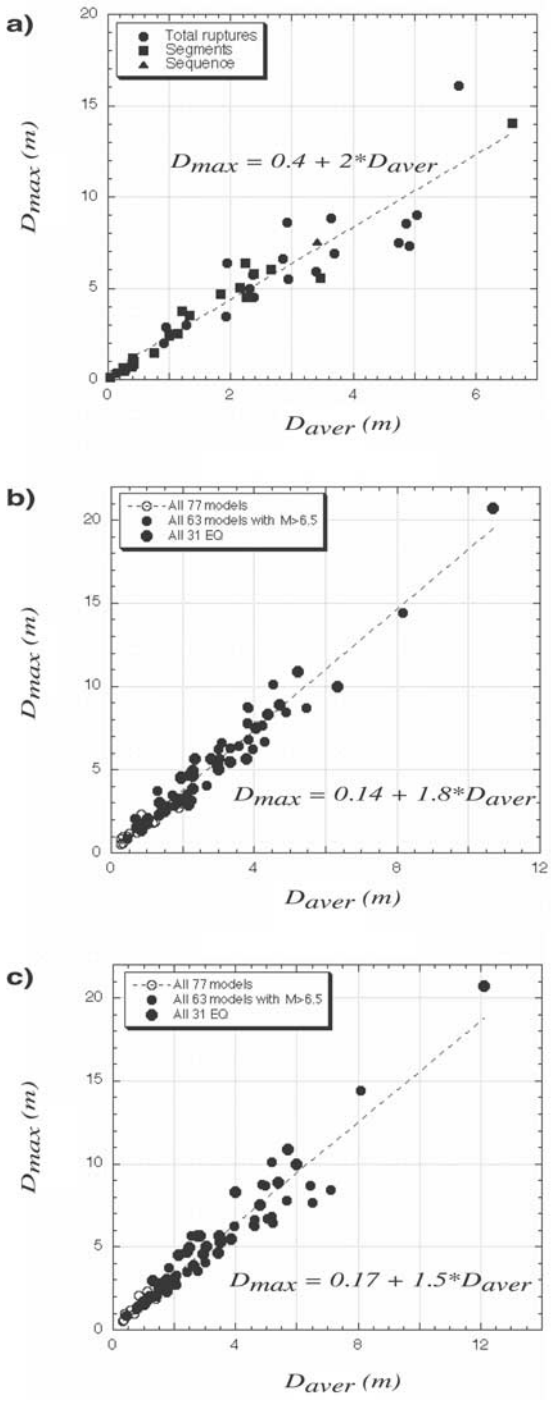

Figure 10. Plot of maximum (D_{max}) versus average (D_{aver}) displacement for the slip profiles analyzed. (a) Surface slip profiles from Table 1. (b) Along-strike maximum slip profiles from models in Table 2. (c) Along-dip maximum slip profiles from models in Table 2. Models with D_{max} > 21 m (i.e., unrealistic) are excluded from calculations. Ratio for along-dip profiles is slightly <2 because distribution of slip along fault width is quite poorly constrained.

data). Similarly, the Y axis is the along-dip distance (HA_z) between an hypocenter and the apex of the reference triangle that best fits the along-dip maximum slip profile of its corresponding earthquake (same remark). Distances are given in percent of L_{obs} and W_{obs}. Symbols are as before, with their surface proportional to magnitude. Symbol shapes indicate the degree of asymmetry of the slip profiles (see Figure 12 caption). Note that most hypocenters that fall on the X or Y axes come from teleseismic models (Table 3). Those are generally unable to properly constrain the relative positions of hypocenter and centroid. Most of these points may therefore be incorrect.

[28] Figure 12a shows that hypocenters are not evenly distributed within the whole plot. There is one domain where all hypocenters are, and one domain totally free of hypocenters. This suggests that there is a critical distance from a major "asperity" (here taken to be the zone of maximum slip, coinciding with the graph origin)

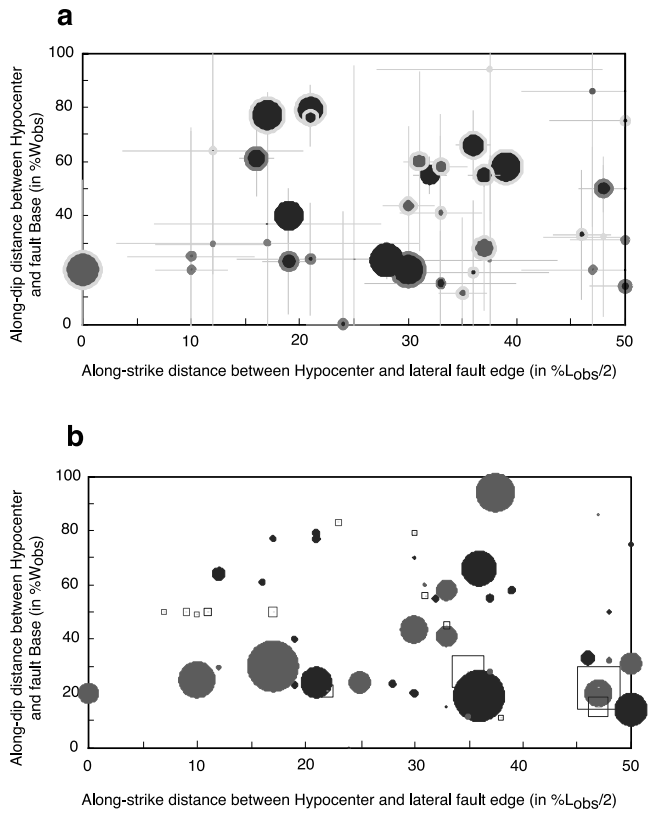

Figure 11. Distribution of hypocenters with respect to fault plane edges. X axis is along-strike position (in percent of L_{obs}) of hypocenters with respect to lateral fault plane edges (irrespective of which side). Y axis is along-dip position (in percent W_{obs}) of hypocenters with respect to fault plane base. Dip-slip and strike-slip faults are in blue and red, respectively. (a) Symbol size proportional to magnitude. Data are from Table 2 (averaged per earthquake; in few cases, best model is preferred). Uncertainties on hypocenter positions are assigned to 5 km in both x and y. Yellow and green circled symbols are for slip profiles tapering downward and upward, respectively. (b) Symbol size proportional to D_{max}/L_{model}. Data are from Tables 2 (solid symbols) and 3 (open symbols). See color version of this figure at back of this issue.

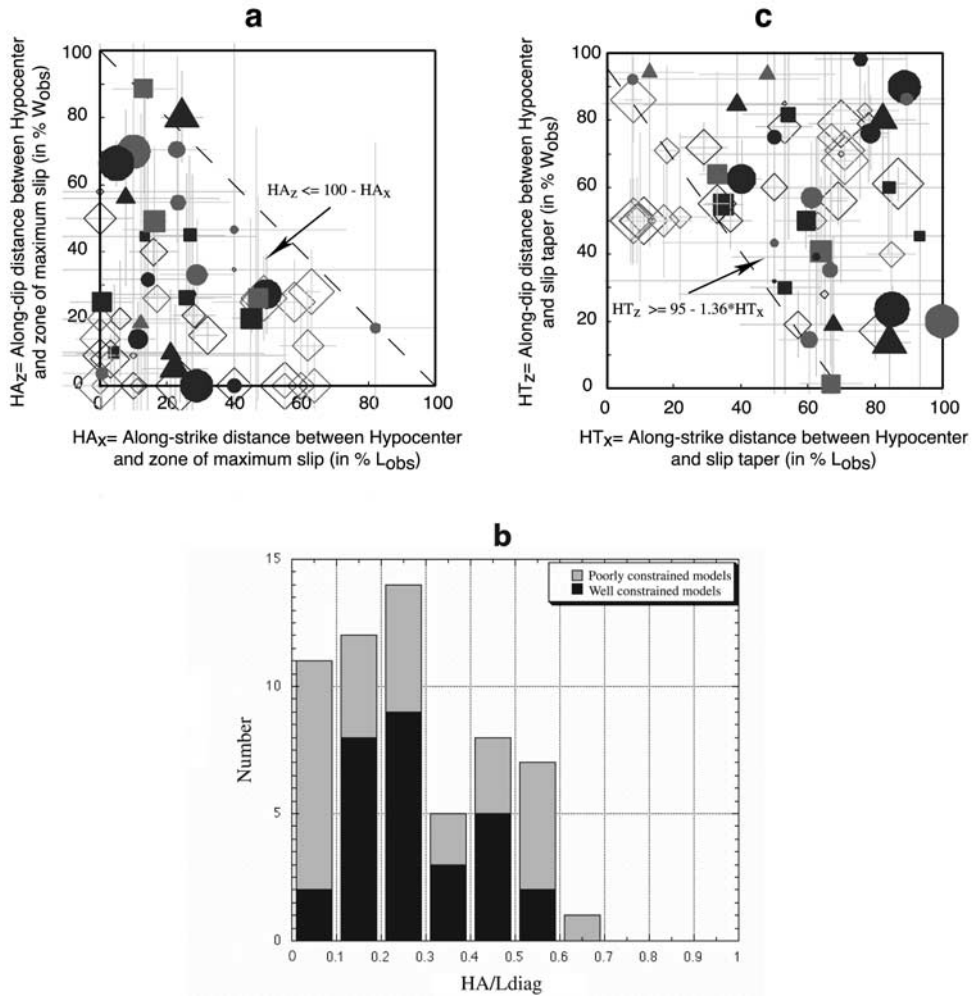

Figure 12. Position of hypocenters (H) with respect to zone of maximum slip (major asperity, A) and to slip taper (T) for earthquake faults with triangular slip profiles (both along strike and dip). Colors and uncertainties are as in Figure 11. Solid symbols are for best constrained models (from Table 2, as in Figure 11); open symbols are for poorly constrained models (from Table 3). Symbol shape indicates degree of asymmetry of along-strike slip profiles. For ruptures wider than 40 km, however, asymmetry is that of along-dip slip profiles. For models with tabular data, distances HA are those between hypocenter and apex of best fitting triangle. For models with no tabular data, distances HA and HT are estimated from visual inspection of the models (when hypocenters lie close to their zone of maximum slip, HA is fixed to zero; open symbols falling on any of the axes are therefore not well constrained). In all plots, symbol size is proportional to magnitude. (a) Position of hypocenter with respect to zone of maximum slip, with distances in percent of L_{obs} and W_{obs}. (b) Histogram of HA ($HA = (Ha_x^2 + Ha_z^2)^{0.5}$, all in km) normalized by diagonal length ($L_{diag} = (L^2 + W^2)^{0.5}$, all in km) of events. (c) Position of hypocenter with respect to slip taper, with distances in percent of L_{obs} and W_{obs}. See color version of this figure at back of this issue.

beyond which an earthquake does not nucleate. The limit separating the two domains is not clear, but we note that all hypocenters lie below a straight line. Any rupture nucleating quite far (in percent of L_{obs} or W_{obs}) in one direction from a major asperity apparently needs to be much closer from it in the perpendicular direction. The maximum distance (in percent of L_{obs} and W_{obs}) at which an earthquake can nucleate from the major asperity that it eventually breaks is ~50% of its total length and width. Most earthquakes, however, seem to nucleate closer, with a hypocenter asperity distance (HA) on the order of 20–30% of their total length or width. This average value is similar to the mean normalized size of major asperities within earthquake fault planes as determined from smaller data sets by *Somerville et al.* [1999] and *Beresnev and Atkinson* [2002]. This suggests that earthquakes may actually nucleate at the edges of the major asperities that they eventually break. We note that rare are those nucleating in their final zone of peak slip (graph origin; see remark above on teleseismic models). These results are in agreement with those of *Mai et al* [2005], who statistically investigated the hypocenter position in inversion models and found that most ruptures nucleate in or close to regions of large slip.

[29] The size of the "major asperities" (taken to be the distance HA) broken by the earthquakes can be examined in

Figure 12b. Figure 12b is a histogram of these HA normalized by the diagonal length of the rupture planes. It confirms that in most cases HA averages 20–30% of the rupture size, whatever that size (i.e., earthquake magnitude) is. This makes HA scaling with the earthquake moment roughly as L does. Note that a similar result has been suggested by *Aki* [1992], *Somerville et al.* [1999], *Beresnev and Atkinson* [2002], and *Mai and Beroza* [2002]. Finally, we observe that HA never is greater than 60–70% of the rupture length. This suggests that earthquakes break larger surfaces than those of their major asperities.

3.2.3. Position of Hypocenters With Respect to Slip Tapers

[30] We here look for a possible relationship between the place where earthquakes initiate (hypocenters) and the place where they gently die out (gentle slip tapers). Figures 12c is similar to 12a, except that it shows the position of hypocenters with respect to the tapers of the triangular slip profiles (distances HT_x and HT_z; note that those are not necessarily complementary to HA_x and HA_z). If one omits the few poorly constrained models with a hypocenter arbitrarily located at half fault width, two different domains again appear, one where all hypocenters are, the other free of any. This suggests that an earthquake that would nucleate close to its slip taper in one direction (as Landers, Denali etc...), would nucleate far from its slip taper in the other direction (hence close to its zone of peak slip; note that "distances" are expressed in percent of L_{obs} and W_{obs}). All in all, earthquakes nucleate at distances from their tapers that are greater than their half length and width together. This shows that significant portions of the fault surfaces, i.e., those with low slip roughly linearly tapering to zero, cannot be the site of rupture initiation. This suggests that these portions are far from their rupture threshold when the earthquake nucleates. We will come back to this point in the discussion.

3.3. Analyzing the Scaling Relations for the Available Earthquakes

[31] The observation of slip profiles being similar in shape for the whole range of scales and focal mechanisms analyzed, suggests that slip distributions on earthquake faults are self-similar, i.e., scale invariant in the range of scales considered in this study. If this is true, the profiles of maximum slip should have their maximum displacement value (D_{max}) scaling roughly linearly with their length (either L or W). We address this question here. So far, a lot of studies have been carried out to determine whether or not mean slip would scale with rupture width or length, that is, stress drop would be independent of earthquake size or not [*Scholz*, 1982; *Romanowicz*, 1992; *Scholz*, 1994a, 1994b; *Bodin and Brune*, 1996; *Mai and Beroza*, 2000; *Shaw and Scholz*, 2001] (see *Scholz* [2002] for a review). After 20 years of debate (and of accumulating data), it now seems that all earthquakes but the largest ones are self-similar, i.e., have stress drops roughly constant overall (in the hypothesis of elastic cracks [e.g., *Scholz*, 2002]). In other words, for small and moderate earthquakes, D_{mean} scales roughly linearly with W, while increasing asymptotically with L. For the largest earthquakes, mean slip is suggested to saturate to an about constant value.

[32] Here, we use our data sets to further document this behavior. However, we only focus on the relations between D_{max} and L and W (for D_{mean} is poorly documented in our data sets, as in most data sets used before). For triangular profiles, however, $D_{max} = 2D_{mean}$ (see Figure 10) so that any conclusion drawn on D_{max}/L (or W) scaling applies to mean displacement length (or width) scaling as well. While surface measurements are well constrained, they generally only represent a fraction of the total slip (and length) on the rupture planes. By contrast, while slip maps inferred from inversions do not include all the details of the ruptures, they contain their main features at depth, both in terms of slip amplitude and spatial extension. We therefore combine these two data types to shed light on possible differences of scaling laws from depth to surface. For the inversion models, we use the original values of slip (D_{max} and D_{mean}) and dimensions (L_{model} and W_{model}) (to preserve seismic moment; Table 2). Where several models exist for an earthquake, we consider the averaged slip, length and width values (unrealistic values are excluded; see Table 2 and ES01). For surface data, we use L_{obs}. Hence, as length notations are different for the various data sets, lengths are simply referred to as L in the following.

[33] Figures 13a–13b plot D_{max} as a function of L for dip-slip and strike-slip earthquakes, respectively (see Figure 13 caption for details). Although the distribution of dip-slip data is not completely clear, it shows the same tendencies as described before [e.g., *Scholz*, 2002]; that is, maximum slip roughly linearly scales with length for earthquakes with $L \leq 100–150$ km. For longer ruptures, there is no evidence of a systematic increase of D_{max} with L, the maximum slip saturating at 4 ± 2 m in most cases. The distribution of strike-slip data is different. The population of measurements defines three major trends, with very few data in between. The steepest trend coincides with that defined for short dip-slip ruptures. Along each trend, D_{max}/L is roughly constant (or slightly decreasing with length). In a following paper, we will show that earthquakes falling on one trend or another pertain to different tectonic regions, with different lithospheric thicknesses.

[34] Figure 13c shows D_{max} as a function of W for all available data (less numerous than before as W is rarely known). It suggests that for most ruptures (dip slip and strike slip) with $W \leq 30–40$ km, D_{max} roughly scales with W. Note that these "constant stress drop ruptures" include most major strike-slip earthquakes. For wider ruptures ($W \geq 30–40$ km; here they are the largest dip-slip earthquakes), there is no clear trend of linear scaling, suggesting that stress drop deduced from the simple crack model is no longer constant for these ruptures.

[35] The analysis above therefore confirms that all dip-slip and strike-slip earthquakes worldwide but the largest ones (= with L > 150 km and/or W > 40 km) obey self-similar scaling. Their ratios D_{max}/L and D_{max}/W are about constant (so their stress drops if they behave as elastic cracks), so that their along-strike and along-dip triangular slip profiles are self-similar. For largest strike-slip earthquakes, D_{max}/L is roughly constant along each of the three major trends observed. This makes the along-strike triangular slip profiles self-similar in shape along each given trend. D_{max} instead saturates for increasing W (largest dip-slip earthquakes), suggesting that along-dip

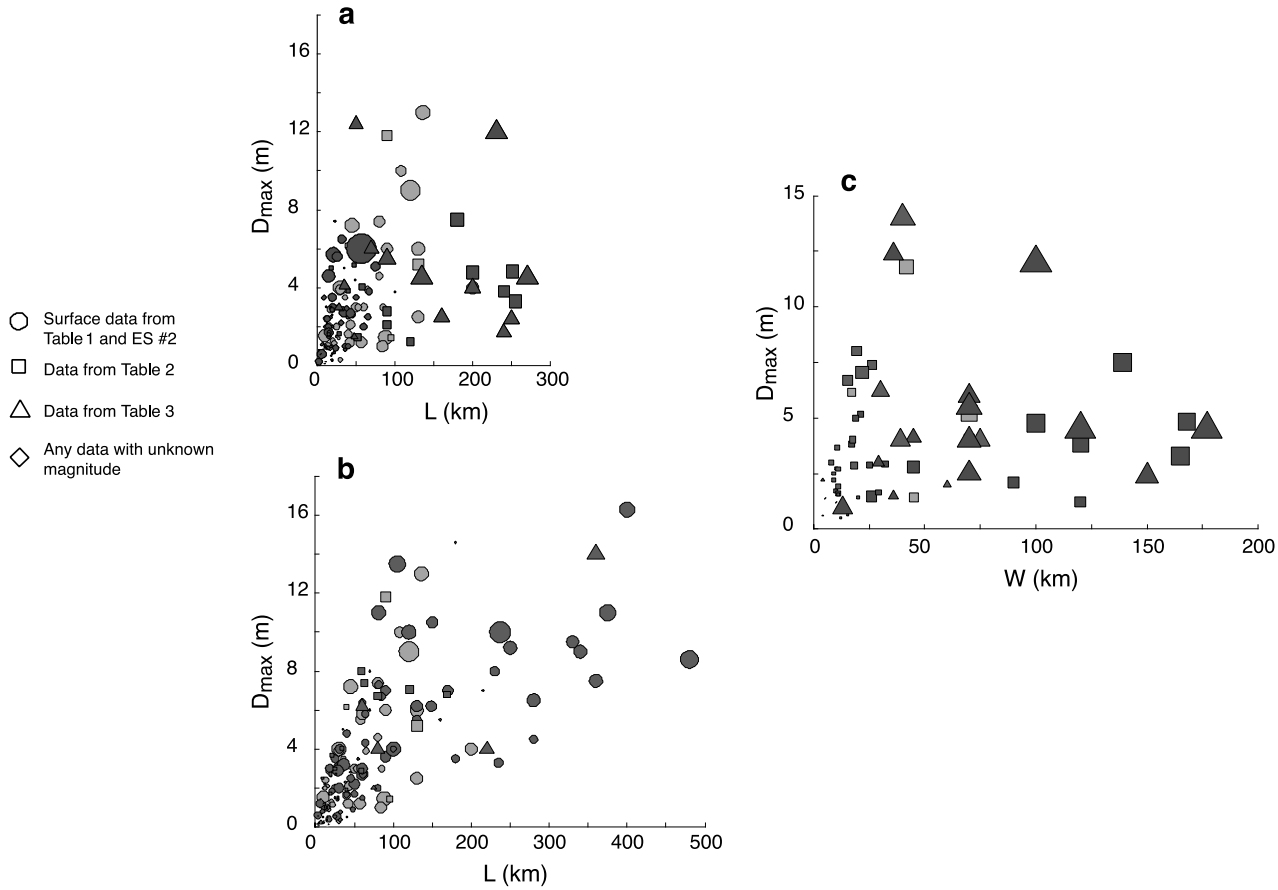

Figure 13. Scaling relations for the earthquakes analyzed. (a) Maximum displacement (D_{max}) versus length (L) for dip-slip (blue) and oblique (gray) faults (from Tables 1, 2, and 3 and ES02). (b) Maximum displacement (D_{max}) versus length (L) for strike-slip (red) and oblique (gray) faults (from Tables 1, 2, and 3 and ES02). (c) Maximum displacement (D_{max}) versus width (W) for dip-slip (blue), strike-slip (red), and oblique (gray) faults (from Tables 2 and 3). Symbol size is proportional to magnitude. Where that is unknown (as for earthquake sequences), symbol size is set to an arbitrary value (corresponding to M = 6). L is L_{obs} for data from Table 1, L_{meas} for data from ES022, and L_{model} for data from Tables 2 and 3 (same for W). See color version of this figure at back of this issue.

slip profiles on major dip-slip faults are not self-similar in shape.

4. Comparison Between Seismic and Cumulative ($\sim 10^{-2}$ to 1 Ma) Slip Profiles

[36] So far we have examined a large number of earthquakes together and showed that this reveals common general properties of the coseismic slip on individual earthquake ruptures. With time, earthquakes repeat on a given fault and make it grow. Their individual slip profiles add to produce a total "cumulative" slip distribution on the fault. Provided that a large number of earthquakes is involved, the cumulative slip distributions therefore give an over time-averaged image of earthquakes. Hence, if earthquakes have general properties, those should appear in these cumulative slip distributions as well. We investigate this point below.

[37] It has long been shown that maximum displacement on long-term faults roughly linearly scales with their length, so that cumulative faults grow self-similar (whether they are strike slip or dip slip [e.g., *Manighetti et al.*, 2001; *Peacock*, 2002; *Scholz*, 2002, and references therein]). In the framework of elastic mechanics, such self-similarity is in agreement with faults growing by developing elliptical (or bell-shaped, that is with local tapers at their tips) cumulative slip profiles. This is why slip distributions on long-term faults have long been predicted and taken to be elliptical in shape [e.g., *Scholz*, 1990; *Cowie and Scholz*, 1992a, 1992b]. Yet, real measurements of cumulative slip profiles show that this is rarely the case [e.g., *Manighetti et al.*, 2001, and references therein; *Scholz*, 2002]. *Manighetti et al.* [2001] measured ~250 cumulative slip profiles on active normal faults and systems (Afar, East Africa) spanning a broad range of scales ($L = 1–10^2$ km; $D_{max} = 1–10^3$m) and ages (10^{-1} to 1 Ma; note that these ages imply that each fault has accumulated hundreds to thousands of earthquakes). Eighty-five percent of these profiles were found to be triangular in overall shape, and most of them were found to be asymmetric (64% over the 85%; see discussion by *Manighetti et al.* [2001]). The overall pattern most commonly found is shown in Figure 14 (stacking of ~80 profiles; see Figure 14 caption for details). It is similar to that that we found for seismic slip profiles (compare

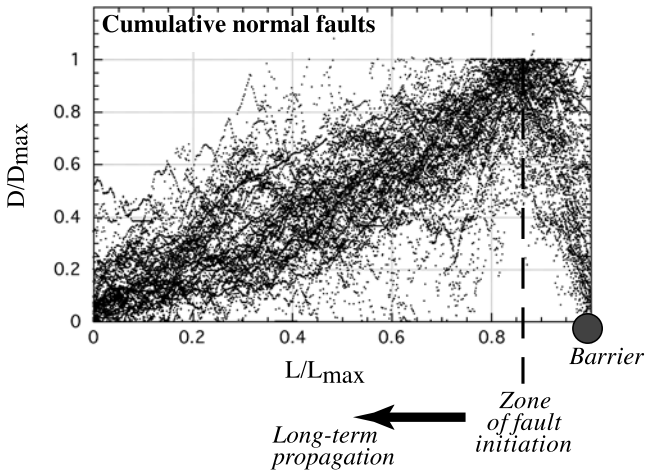

Figure 14. Overall slip distribution pattern on long-term normal faults. Plot shows ~80 cumulative slip profiles measured on normal faults of various ages (10^{-1}–1 Ma), lengths (L = 1–10^2 km), and displacements (D = 1–10^3 m). Profiles have been normalized by both L and D_{max} with some of them being flipped so that maximum slip is at right [from *Manighetti et al.*, 2001].

Figure 14 to Figures 2, 5, and 7). Although much more rare, the few slip (or slip rate) profiles that have been measured on strike-slip and reverse cumulative faults exhibit the same overall pattern. For instance, the long-term slip rates (10^{-2}–10^{-1} Ma) measured on the ~2000-km-long Altyn Tagh fault show an approximately regular decrease from a maximum value at about the fault center to zero (or almost) at the eastern fault end [*Tapponnier et al.*, 2001]. The cumulative (10^{-2}–10^{-1} Ma) slip distribution on that major strike-slip fault is therefore expected to be triangular (possibly symmetric). Similarly, the slip measurements that were performed on the ~40-km-long Quaternary Puente Hills reverse fault system [*Shaw et al.*, 2002] reveal triangular profiles, both on individual fault segments and on total fault system. Together these observations suggest that cumulative slip profiles on long-term faults are triangular in overall shape (with most of them asymmetric), regardless of fault scale, age, kinematics, location. They therefore resemble those on individual earthquakes. This confirms that considering a long time-averaged accumulation of earthquakes leads to smooth individual earthquake slip complexities and point out a common, general property that is the same than the one that emerged from the combination of a large number of events. That features created in tens of seconds and in tens of thousands to millions years resemble each other suggests that these features share common mechanical explanations.

5. Summary and Discussion

5.1. Summary of Major Observations

[38] We summarize our major observations before discussing them at greater length. We basically found the following:

[39] 1. While earthquakes are complex features with highly heterogeneous mechanical conditions on their planes (due to prestresses, static and dynamic stress loading/unloading by neighboring ruptures, host rock properties, etc.), they share some common, generic properties that appear when a large number of events are examined together: Most produce roughly triangular slip profiles (~70% are asymmetric) with well-defined, long linear tapers of the size of that of the event.

[40] 2. Cumulative faults, which result from the long-term addition of earthquakes (hence provide an over time-averaged image of seismic events), reveal the same property: Most grow by developing triangular and asymmetric slip profiles, with long linear tapers of the size of the fault.

[41] 3. Triangular slip distributions on earthquake faults (but the largest dip-slip ones) seem to be self-similar (in the range of scales analyzed), suggesting that they attest to a scale-invariant mechanical behavior.

[42] 4. That earthquake slip profiles are triangular along both strike and dip implies that seismic ruptures have one single zone of maximum slip and hence break one "major asperity" that is much larger than any others.

[43] 5. Most earthquakes do not nucleate in their zone of maximum slip but commonly nucleate at a distance from it that averages 20–30% of their total length. That distance likely measures the size of the major asperity; most earthquakes would therefore nucleate at the edge of the major asperity that they eventually break.

[44] 6. Most slip profiles are asymmetric, suggesting different behaviors at the two edges of the major asperity. The zone where slip abruptly drops to zero may be where the earthquake was stopped when encountering a rapid change of conditions, while the zone where slip gently tapers to zero may be where the rupture "passively" died out (damping zone). This vision is somehow similar to that of *King* [1986] and *Ward* [1997].

[45] 7. Earthquakes never nucleate in their "taper portions" (if they do so along strike, they do not along dip; or the opposite). This shows that significant fractions of the rupture planes would not have broken if not dynamically loaded.

5.2. Discussion of Major Observations

[46] We found that earthquakes break one major asperity only whose size is ≈a third of the total event size. What are the parameters that determine such asperity size, i.e., the size of the earthquake? In other words, does the distribution of slip entirely result from the dynamic process and the stress conditions (widely unknown at depth), or is the process controlled by some preexisting geological structures? In the latter case, earthquake hazard evaluation would strongly benefit from the identification of the tectonic (or any other) structures defining the potential major asperities. In the former case, earthquakes would remain deterministically unpredictable.

[47] Geological observations may help answering this question. ES06 describes the main features that were observed about where the 56 listed earthquakes initiated (column 5), had their maximum slip abruptly dropping to zero (column 6), and had their slip gently tapering to zero (column 7). Note that while aspects of these observations have been touched on by a number of authors [e.g., *Segall and Pollard*, 1980; *King*, 1986; *Sibson*, 1985, 1986; *Scholz*, 1990; *Harris et al.*, 1991; *Harris and Day*, 1993; *Kame and Yamashita*, 1999; *Oglesby and Day*, 2001; *Harris et al.*,

2002; *Das*, 2003], we have here compiled them for many more earthquakes than has been done before. That compilation reveals that most earthquakes initiated at or close to an intersection between two strongly oblique faults (in strike and in some cases also in dip), one eventually broke during the earthquake. It also shows that most earthquakes have their slip abruptly dropping to zero also at or close to where their plane intersects a strongly oblique fault (in strike or dip). Hence most earthquakes both initiate and abruptly stop at specific spots that bound, and hence define the major asperity, and are controlled by the preexisting fault geometries. The size of the major asperity (i.e., distance HA for the approximately two thirds of earthquakes that have asymmetric profiles) is thus controlled by factors preexisting the event, as the geometry of the fault itself or the presence of surrounding fault systems. The structural/mechanical discontinuities on and around faults exist at a broad range of scales, resulting in a similarly large range of earthquake sizes.

[48] As zones where oblique faults intersect may sustain higher stress concentrations than the surrounding medium [e.g., *King*, 1983, 1986; *Archuleta*, 1984], they may be close to their rupture threshold and capable to favor rupture nucleation. If the medium around is stressed at a ''sufficiently'' high level (or with sufficient connectivity between high-stress patches [e.g., *Nielsen and Olsen*, 2000; *Miller*, 2002]), the rupture may start propagating and growing. If the stress environment is favorable, the rupture is not supposed to stop [e.g., *Scholz*, 2002]. The arrest of the rupture can be produced, however, either by a strong region that is capable of sustaining high stresses without breaking (e.g., crosscutting fault unfavorably oriented for rupture, regions of tough rocks, zones where stresses have been relaxed by previous earthquakes or creep [e.g., *Aki*, 1979; *Rice*, 1980; *Sibson*, 1989]), or by a region weak enough to have accommodated the tectonic load (e.g., regions of soft material such as active volcanoes, densely fissured and faulted areas [e.g., *Husseini et al.*, 1975; *Boatwright and Cocco*, 1996]). These arresting features have long been observed and indifferently referred to as ''barriers'' [e.g., *Aki et al.*, 1978; *King*, 1983; *King and Yielding*, 1984; *King and Nabelek*, 1985; *King*, 1986; *Sibson*, 1989; *Wesnousky*, 1988, 1994; *Susong et al.*, 1990; *Poliakov et al.*, 2002; *Das*, 2003]. ES06 suggests that zones where oblique faults intersect can act as barriers. Other features are observed, however, which act similarly (step over areas, zones in which stresses have been relaxed by a previous earthquake, etc). Hence barriers exist at many scales. Yet, *Zhang et al.* [1999] [see also *King*, 1983; *Sibson*, 1989; *Lettis et al.*, 2002] have shown that the size of those capable of arresting earthquakes is related to these earthquake magnitudes.

[49] By contrast with the abrupt stop discussed above, in general, no particular features are observed where slip gently tapers to zero (ES06). Hence earthquakes can fade away anywhere along the faults. We also showed that earthquakes never nucleate within their ''low slip areas'' (corresponding to slip tapers both in strike and dip). This shows that these low slip areas of the rupture planes were not in the appropriate stress and/or energetic conditions to break when the earthquake initiated. Hence these portions likely started to break when their stress level was raised by dynamic overshoot [e.g., *Das and Aki*, 1977; *Mikumo and Miyatake*, 1978; *Day*, 1982]. We suggest that some and perhaps most portions of the fault plane extending outside of the major asperity (as defined above) broke when rupture of that asperity had released energy and increased stress enough to make them breakable despite of their unfavorable local energy balance. This scenario has been suggested by the dynamic modeling of *Favreau and Archuleta* [2003].

[50] The triangular slip profiles may therefore result from an ''energetic scenario'': An earthquake would initiate at some high-stress spot (commonly, an intersection zone between two oblique faults) and then grows in length, slip, and magnitude until a mechanical/structural barrier (commonly another fault intersection, but other features are possible; see ES06) stops its lateral propagation. The area broken during this ''first stage'' appears as the major asperity that shapes the total triangular slip distribution. Most of the moment is released by rupture of this area [see also *McGarr and Fletcher*, 2002]. This rupture produces dynamic stress overshoot in the surrounding fault plane. This overshoot makes some unfavorably stressed (or in inappropriate energetic conditions) portions of the fault plane in conditions to slip. The linear trends in the final slip profile are taken to be associated with the progressive dissipation of the energy provided by the dynamic rupture of the main asperity.

[51] In systems of parallel faults, linear slip tapers may result from elastic interaction (e.g., *Scholz* [2002] and S. Wolf et al. (Mechanics of normal fault networks subject to slip weakening friction, submitted to *Geophysical Journal International*, 2004) for a dynamic model). Stress shadowing effects cannot be put forward, however, when considering that major faults at large scale are isolated. It is difficult to reproduce triangular slip profiles on large earthquakes with present-day models without having ad hoc hypotheses on the distributions of friction properties or of stress. Since the triangular shape appears from averaging a large number of events, it must result from robust physical properties, not from peculiarities of initial conditions. We suggested above that the linear trends may be associated with the progressive dissipation of the energy provided by the dynamic rupture of the main asperity in regions that were not prone to slip. The self-similarity of the slip distributions implies that such dissipation is a scale-dependent process. This conclusion goes against the classical use of constant friction laws on faults embedded in elastic bodies.

[52] ES06 describes the features that are observed or evidenced around the low slip portions (tapers, i.e., damping zones) of the listed earthquakes (column 8). It shows that for most events, coseismic (or immediately postseismic) off-fault deformation is observed around the zones of low slip, mainly as secondary oblique faults slipping together with the main rupture (and generally continuing slipping during the few years following the earthquake), crack opening, distributed off-fault earthquakes (some are possibly coseismic) with high-stress drops and mechanisms differing from that of the main rupture. In most cases, these zones of off-fault deformation are large (several kilometers). It is therefore possible that a significant fraction of the dynamic energy dissipates in the surrounding medium (as suggested by *Poliakov et al.* [2002] and *McGarr and Fletcher* [2002]) through off-fault slip or ''damage.'' Here we use the term damage in a much broader sense than

commonly done, as we consider that any off-fault deformation of the volume, pervasive or localized, plastic or elastic, of microscopic to macroscopic scale, can act as damage. Permanent (static) damage (used in the same broad sense) has been recently evoked to explain the development of self-similar triangular slip profiles on cumulative faults [*Manighetti et al.*, 2004]. Such permanent damage would accommodate the excess stresses that a triangular slip distribution would otherwise produce on the main fault plane. This would allow faults to grow in a self-similar way (i.e., homogeneous stress distribution on their plane) while maintaining triangular slip profiles. Introducing off-fault damage in the dynamic rupture models has rarely been done [*Dalguer et al.*, 2003; *Andrews*, 2005], but we suggest that it may be part of the key to understand why earthquake slip profiles are triangular. Dissipation in the volume around the earthquake faults could also help understanding better the friction and heat flow paradox [e.g., *Brune et al.*, 1969; *Scholz*, 2000; *Ben-Zion*, 2001; *Das*, 2003]. Also, if damage occurs preferentially on one side of the ruptures, as ES06 suggests, it may contribute to generate material contrasts on either sides of the fault. This could in turn partly explain why most earthquakes propagate unilaterally [*McGuire et al.*, 2002].

6. Conclusions

[53] We have investigated what slip distributions look like on earthquake faults. We addressed this issue by considering slip distributions on earthquakes large enough for the local perturbations at their tips to be neglected. We analyzed two types of data. On one hand, we compiled 44 slip profiles measured by geologists at the surface after major earthquakes of various focal mechanisms and magnitudes. On the other hand, we derived along-strike and along-dip slip profiles from 76 slip inversion models obtained by inversion of seismological and/or geodetic data for various earthquakes. We investigated the overall shape of these slip profiles, and found that these are basically triangular (for ~90% of the profiles), and most of them (70–80%) strongly asymmetric. We then compared these earthquake slip profiles to cumulative slip profiles measured on long-term faults of various ages (10^4–10^6 years), sizes (1–10^3 km), and kinematics and found that they are similar, i.e., overall triangular and asymmetric. This makes slip, whether it is seismic or cumulative, roughly linearly decreasing from a maximum at one fault tip to zero at the other fault tip. High slip gradients and long linear slopes (of the size of the seismic events or of the faults) therefore are the key ingredients to describe slip distributions on earthquake and long-term faults.

[54] The observation of triangular slip distributions therefore attests to a common, general property of faults, regardless of their scale (in space and time, as it applies from "instantaneous" earthquakes to long-term faults) and kinematics. Combining a dense population of earthquakes, or considering a long time-averaged accumulation of earthquakes (cumulative profiles), helps smoothing the individual slip complexities and points out a common, generic property. It appears that although earthquakes are irregular and heterogeneous in detail, they share homogeneous average properties that are similar on a wide range of length scales. Also, although individual earthquakes differ from one another in detail, they combine to produce homogeneous features at a longer timescale (and space scale) (cumulative profiles).

[55] That slip distributions on individual earthquakes are triangular confirms that triangular cumulative slip profiles do not result from the addition of elliptical seismic slip profiles, as it had been proposed [e.g., *Walsh and Watterson*, 1987, 1988; *Peacock and Sanderson*, 1996; *Chang and Smith*, 2002]. Instead, faults grow through the addition of triangular slip functions, and produce similar functions as they grow (we, however, ignore how the entire process works). The triangular slip profiles are furthermore shown to be self-similar, whether they are seismic or cumulative.

[56] Together these demonstrate that the earthquake process involves and produces heterogeneous stress conditions. This prevents the use of oversimplified linear homogeneous models to reproduce the observed generic properties of slip distributions. We suggest that introducing in the volume holding the earthquake ruptures, either plastic deformation or elastic distributed cracking and faulting, both involving nonlinear strain behavior, may be a way to reconcile the earthquake models with the observations.

[57] On average, slip distributions are dominated by one zone of large slip only, whose rupture accounts for most of the moment release. We found that earthquakes nucleate at a finite distance from this zone of maximum slip. That distance averages 20–30% of their total length, and likely measures the size of the major asperity broken by the earthquake. Compiling observations made where past earthquakes initiated and abruptly stopped, suggests that most of these asperities are fault segments or systems extending between two major structural discontinuities, mainly zones of oblique cross cutting faults. Most earthquakes are observed to nucleate where two strongly oblique (commonly roughly perpendicular) faults intersect. Then they propagate and grow unilaterally until they abut another structural discontinuity (a "barrier") after which they progressively die out in the form of long linear slip tapers. If this scenario is correct, it implies that knowing the long-term fault geometry may significantly help earthquake hazard quantitative evaluation.

[58] **Acknowledgments.** This work has been done during the 2 year visit of the first author in the SCEC Department, USC, Los Angeles. The first author particularly thanks Y. Delaby for his help with data processing. We are grateful to R. Dmowska, J. Rice and R. Archuleta for fruitful discussions. We thank J. Gomberg, C. Scholz, and an anonymous reviewer for their constructive comments. This is contribution 894 of SCEC; contribution 1344 of the Institute of Geophysics, ETH Zurich; and contribution 2036 of Institut de Physique du Globe de Paris, France.

References

Abercrombie, R., and J. Mori (1994), Local observations of the onset of a large earthquake: 28 June 1992 Landers, California, *Bull. Seismol. Soc. Am.*, *84*, 725–734.

Abercrombie, R. E., M. Antolik, K. Felzer, and G. Ekstrom (2001), The 1994 Java tsunami earthquake: Slip over a subducting seamount, *J. Geophys. Res.*, *106*, 6595–6607.

Aki, K. (1979), Characterization of barriers on an earthquake fault, *J. Geophys. Res.*, *84*, 6140–6148.

Aki, K. (1992), Higher-order interrelations between seismogenic structures and earthquake process, *Tectonophysics*, *211*, 1–12.

Aki, K., M. Bouchon, B. Chouet, and S. Das (1978), Quantitative prediction of strong motion for a potential earthquake fault, *Ann. Geofis.*, *30*, 341–368.

Akyuz, H. S., R. Hartleb, A. Barka, E. Altunel, G. Sunal, B. Meyer, and R. Armijo (2002), Surface rupture and slip distribution of the 12 November 1999 Duzce earthquake (*M* 7.1), North Anatolian fault, Bolu, Turkey, *Bull. Seismol. Soc. Am.*, *92*, 61–66.

Andrews, D. J. (2005), Rupture dynamics with energy loss outside the slip zone, *J. Geophys. Res.*, *110*, B01307, doi:10.1029/2004JB003191.

Antolik, M., and D. S. Dreger (2003), Rupture process of the 26 January 2001 M_w 7.6 Bhuj India earthquake from teleseismic broadband data, *Bull. Seismol. Soc. Am.*, *93*, 1235–1248.

Antolik, M., A. Kaverina, and D. Dreger (2000), Compound rupture of the great 1998 Antarctic plate earthquake, *J. Geophys. Res.*, *105*, 23,825–23,838.

Archuleta, R. J. (1984), A faulting model for the 1979 Imperial Valley earthquake, *J. Geophys. Res.*, *89*, 4559–4585.

Barenblatt, G. I. (1962), The mathematical theory of equilibrium cracks in brittle fracture, *Adv. Appl. Mech.*, *7*, 55–80.

Barka, A. (1996), Slip distribution along the north Anatolian fault associated with the large earthquakes of the period 1939 to 1967, *Bull. Seismol. Soc. Am.*, *86*, 1238–1254.

Barka, A., et al. (2002), The surface rupture and slip distribution of the 17 August 1999 Izmit earthquake (*M* 7.4), North Anatolian fault, *Bull. Seismol. Soc. Am.*, *92*, 43–60.

Bennett, R. A., R. E. Reilinger, W. Rodi, Y. Li, M. N. Toksöz, and K. Hudnut (1995), Coseismic fault slip associated with the 1992 M_w 6.1 Joshua Tree, California, earthquake: Implications for the Joshua Tree-Landers earthquake sequence, *J. Geophys. Res.*, *100*, 6443–6462.

Ben-Zion, Y. (2001), Dynamic ruptures in recent models of earthquake faults, *J. Mech. Phys. Solids*, *49*, 2209–2244.

Berberian, M., et al. (2001), The 1998 March 14 Fandoqa earthquake (M_w 6.6) in Kerman province, southeast Iran: Re-rupture of the 1981 Sirch earthquake fault, triggering of slip on adjacent thrusts and the active tectonics of the Gowk fault zone, *Geophys. J. Int.*, *146*, 371–398.

Beresnev, I. A., and G. M. Atkinson (2002), Source parameters of earthquakes in eastern and western North America based on finite-fault modeling, *Bull. Seismol. Soc. Am.*, *92*, 695–710.

Beroza, G. C. (1991), Near source modeling of the Loma Prieta earthquake: Evidence for heterogeneous slip and implications for earthquake hazard, *Bull. Seismol. Soc. Am.*, *81*, 1603–1621.

Beroza, G. C., and P. Spudich (1988), Linearized inversion for fault rupture behavior; application to the 1984 Morgan Hill California earthquake, *J. Geophys. Res.*, *93*, 6275–6296.

Boatwright, J., and M. Cocco (1996), Frictional constraints on crustal faulting, *J. Geophys. Res.*, *101*, 13,895–13,909.

Bodin, P., and J. N. Brune (1996), On the scaling of slip with rupture length for shallow strike-slip earthquakes: Quasi-static models and dynamic rupture propagation, *Bull. Seismol. Soc. Am.*, *86*, 1292–1299.

Bouchon, M., N. Toksöz, H. Karabulut, M. Bouin, M. Dietrich, M. Aktar, and M. Edie (2000), Seismic imaging of the 1999 Izmit (Turkey) rupture inferred from the near-fault recordings, *Geophys. Res. Lett.*, *27*, 3013–3016.

Bouchon, M., M. N. Toksoz, H. Karabulut, M. P. Bouin, M. Dietrich, M. Aktar, and M. Edie (2002), Space and time evolution of rupture and faulting during the 1999 Izmit (Turkey) earthquake, *Bull. Seismol. Soc. Am.*, *92*, 256–266.

Brune, J., T. Henyey, and R. Roy (1969), Heat flow, stress, and rate of slip along the San Andreas fault, California, *J. Geophys. Res.*, *74*, 3821–3827.

Campillo, M., and R. J. Archuleta (1993), A rupture model for the 28 June 1992 *M*7.4 Landers, California, earthquake, *Geophys. Res. Lett.*, *20*, 647–650.

Caskey, S. J., and S. G. Wesnousky (1997), Static stress changes and earthquake triggering during the 1954 Fairview Peak and Dixie Valley earthquakes, central Nevada, *Bull. Seismol. Soc. Am.*, *87*, 521–527.

Caskey, S. J., S. G. Wesnousky, P. Zhang, and D. B. Slemmons (1996), Surface faulting of the 1954 Fairview Peak (M_s 7.2) and Dixie Valley (M_s 6.8) earthquakes, central Nevada, *Bull. Seismol. Soc. Am.*, *86*, 761–787.

Chambon, G., and J. W. Rudnicki (2001), Effects of normal stress variations on frictional stability of a fluid-infiltrated fault, *J. Geophys. Res.*, *106*, 11,353–11,372.

Chang, W. L., and R. B. Smith (2002), Integrated seismic-hazard analysis of the Wasatch front, Utah, *Bull. Seismol. Soc. Am.*, *92*, 1904–1922.

Chi, W. C., D. Dreger, and A. Kaverina (2001), Finite-source modeling of the 1999 Taiwan (Chi-Chi) earthquake derived from a dense strong-motion network, *Bull. Seismol. Soc. Am.*, *91*, 1144–1157.

Choy, G. L., and J. W. Dewey (1988), Rupture process of an extended earthquake sequence: Teleseismic analysis of the Chilean earthquake of March 3, 1985, *J. Geophys. Res.*, *93*, 1103–1118.

Cohee, B. P., and G. C. Beroza (1994), Slip distribution of the 1992 Landers earthquake and its implications for earthquake source mechanics, *Bull. Seismol. Soc. Am.*, *84*, 692–712.

Cotton, F., and M. Campillo (1995), Frequency domain inversion of strong motions: Application to the 1992 Landers earthquake, *J. Geophys. Res.*, *100*, 3961–3975.

Cowie, P. A., and C. H. Scholz (1992a), Physical explanation for the displacement-length relationship of faults using a post-yield fracture mechanics models, *J. Struct. Geol.*, *14*, 1133–1148.

Cowie, P. A., and C. H. Scholz (1992b), Growth of faults by accumulation of seismic slip, *J. Geophys. Res.*, *97*, 11,085–11,095.

Crone, A. J., and M. N. Machette (1984), Surface faulting accompanying the Borah Peak earthquake, central Idaho, *Geology*, *12*, 664–667.

Dalguer, L. A., K. Irikura, and J. D. Riera (2003), Simulation of tensile crack generation by three-dimensional dynamic shear rupture propagation during an earthquake, *J. Geophys. Res.*, *108*(B3), 2144, doi:10.1029/2001JB001738.

Das, S. (2003), Spontaneous complex earthquake rupture propagation, *Pure Appl. Geophys.*, *160*, 579–602.

Das, S., and K. Aki (1977), A numerical study of two dimensional spontaneous rupture propagation, *Geophys. J. R. Astron. Soc.*, *50*, 643–668.

Das, S., and B. V. Kostrov (1983), Breaking a single asperity: Rupture process and seismic radiation, *J. Geophys. Res.*, *88*, 4277–4288.

Das, S., and B. V. Kostrov (1990), Inversion for seismic slip rate history and distribution with stabilizing constraints: Application to the 1986 Andreanof islands earthquake, *J. Geophys. Res.*, *95*, 6899–6913.

Das, S., and C. H. Scholz (1983), Why large earthquakes do not nucleate at shallow depths, *Nature*, *305*, 621–623.

Day, S. M. (1982), Three dimensional simulation of spontaneous rupture: The effect of non-uniform prestress, *Bull. Seismol. Soc. Am.*, *72*, 1881–1902.

Delouis, B., D. Giardini, P. Lundgren, and J. Salichon (2001), Details of the 1999 Izmit-Düzce (Turkey) mainshock sequence from geodetic and seismological data, paper presented at 26th General Assembly of the European Geophysical Society (EGS), Nice, France.

Delouis, B., D. Giardini, and P. Lundgren (2002), Joint inversion of Insar, GPS, teleseismic and strong-motion data for the spatial and temporal distribution of earthquake slip: Application to the 1999 Izmit mainshock, *Bull. Seismol. Soc. Am.*, *92*, 278–299.

Deng, Q., and P. Zhang (1984), Research on the geometry of shear fracture zones, *J. Geophys. Res.*, *89*, 5699–5710.

Dominguez, S., J. Avouac, and R. Michel (2003), Horizontal coseismic deformation of the 1999 Chi-Chi earthquake measured from SPOT satellite images: Implications for the seismic cycle along the western foothills of central Taiwan, *J. Geophys. Res.*, *108*(B2), 2083, doi:10.1029/2001JB000951.

Dreger, D. S. (1994), Empirical Green's function study of the January 17 1994 Northridge California earthquake, *Geophys. Res. Lett.*, *21*, 2633–2636.

Eberhart-Philipps, D., et al. (2003), The 2002 Denali fault earthquake, Alaska: A large magnitude, slip-partitioned event, *Science*, *300*, 1113–1118.

Favreau, P., and R. J. Archuleta (2003), Direct seismic energy modeling and application to the 1979 Imperial Valley earthquake, *Geophys. Res. Lett.*, *30*(5), 1198, doi:10.1029/2002GL015968.

Feigl, K. L., F. Sarti, H. Vadon, and R. Burgmann (2002), Estimating slip distribution for the Izmit mainshock from coseismic GPS, ERS-1, Radarsat, and SPOT measurements, *Bull. Seismol. Soc. Am.*, *92*, 138–160.

Harris, R. A., and S. M. Day (1993), Dynamics of fault interaction: Parallel strike-slip faults, *J. Geophys. Res.*, *98*, 4461–4472.

Harris, R. A., R. J. Archuleta, and S. M. Day (1991), Fault steps and the dynamic rupture process: 2D numerical simulations of a spontaneously propagating shear fracture, *Geophys. Res. Lett.*, *18*, 893–896.

Harris, R. A., J. Dolan, R. Hartleb, and S. M. Day (2002), The 1999 Izmit Turkey earthquake: A 3D dynamic stress transfer model of intraearthquake triggering, *Bull. Seismol. Soc. Am.*, *92*, 245–255.

Hartleb, R. D., et al. (2002), Surface rupture and slip distribution along the Karadere segment of the 17 August 1999 Izmit and the western section of the 12 November 1999 Duzce, Turkey, earthquakes, *Bull. Seismol. Soc. Am.*, *92*, 67–78.

Hartzell, S., and C. Langer (1993), Importance of model parameterization in finite fault inversions: Application to the 1974 M_W 8.0 Peru earthquake, *J. Geophys. Res.*, *98*, 22,123–22,134.

Hartzell, S., C. Lenger, and C. Mendoza (1994), Rupture histories of eastern North American earthquakes, *Bull. Seismol. Soc. Am.*, *84*, 1703–1724.

Hartzell, S., P. Liu, and C. Mendoza (1996), The 1994 Northridge, California, earthquake: Investigation of rupture velocity, risetime, and high-frequency radiation, *J. Geophys. Res.*, *101*, 20,091–20,108.

Hartzell, S. H. (1989), Comparison of seismic waveform inversion results for the rupture history of a finite fault: Application to the 1986 North Palm Springs, California, earthquake, *J. Geophys. Res.*, *94*, 7515–7534.

Hartzell, S. H., and T. H. Heaton (1983), Inversion of strong ground motion and teleseismic waveform data for the fault rupture history of the 1979 Imperial Valley California earthquake, *Bull. Seismol. Soc. Am.*, *73*, 1553–1583.

Hartzell, S. H., and T. H. Heaton (1986), Rupture history of the 1984 Morgan Hill California earthquake from the inversion of strong motion records, *Bull. Seismol. Soc. Am.*, *76*, 649–674.

Hartzell, S. H., and C. Mendoza (1991), Application of an iterative least-squares waveform inversion of strong-motion and teleseismic records to the 1978 Tabas Iran earthquake, *Bull. Seismol. Soc. Am.*, *81*, 305–331.

Heaton, T. H. (1982), The 1971 San Fernando earthquake: A double event?, *Bull. Seismol. Soc. Am.*, *72*, 2037–2062.

Hemphill-Haley, M. A., and R. J. Weldon II (1999), Estimating prehistoric earthquake magnitude from point measurements of surface rupture, *Bull. Seismol. Soc. Am.*, *89*, 1264–1279.

Henry, C., and S. Das (2002), The M_w 8.2, 17 February 1996 Biak, Indonesia, earthquake: Rupture history, aftershocks, and fault plane properties, *J. Geophys. Res.*, *107*(B11), 2312, doi:10.1029/2001JB000796.

Hernandez, B., F. Cotton, and M. Campillo (1999), Contribution of radar interferometry to a two-step inversion of the kinematic process of the 1992 Landers earthquake, *J. Geophys. Res.*, *104*, 13,083–13,099.

Hernandez, B., N. M. Shapiro, S. K. Singh, J. F. Pacheco, F. Cotton, M. Campillo, A. Iglesias, V. Cruz, J. M. Gómez, and L. Alcántara (2001), Rupture history of September 30, 1999 intraplate earthquake of Oaxaca, Mexico (M_W = 7.5) from inversion of strong-motion data, *Geophys. Res. Lett.*, *28*, 363–366.

Hough, S. E., and D. S. Dreger (1995), Source parameters of the 23 April 1992 M 6.1 Joshua Tree California earthquake and its aftershocks: Empirical Green's function analysis of GEOS and TERRAscope data, *Bull. Seismol. Soc. Am.*, *85*, 1576–1590.

Huc, M., R. Hassani, and J. Chéry (1998), Large earthquake nucleation associated with stress exchange between middle and upper crust, *Geophys. Res. Lett.*, *25*, 551–554.

Hudnut, K., L. Seeber, T. Rockwell, J. Goodmacher, R. Klinger, S. Lindvall, and R. McElwain (1989), Surface ruptures on cross-faults in the 24 November 1987 Superstition Hills California earthquake sequence, *Bull. Seismol. Soc. Am.*, *79*, 282–296.

Hudnut, K. W., Z. Shen, M. Murray, S. McClusly, R. King, T. Herring, B. Hager, Z. Feng, P. Fang, A. Donnellan, and Y. Block (1996), Coseismic displacements of the 1994 Northridge California earthquake, *Bull. Seismol. Soc. Am.*, *86*, 19–36.

Husseini, M. I., D. B. Jovanovich, M. J. Randall, and L. B. Freund (1975), The fracture energy of earthquakes, *Geophys. J. R. Astron. Soc.*, *43*, 367–385.

Ida, Y. (1972), Cohesive force across tip of a longitudinal shear crack and Griffith's specific energy balance, *J. Geophys. Res.*, *77*, 3796–3805.

Ide, S. (1999), Source process of the 1997 Yamaguchi, Japan, earthquake analyzed in different frequency bands, *Geophys. Res. Lett.*, *26*, 1973–1976.

Ide, S., M. Takeo, and Y. Yoshida (1996), Source process of the 1995 Kobe earthquake: Determination of spatio-temporal slip distribution by Bayesian modeling, *Bull. Seismol. Soc. Am.*, *86*, 547–566.

Ihmlé, P. F. (1998), On the interpretation of subevents in teleseismic waveforms: The 1994 Bolivia deep earthquake revisited, *J. Geophys. Res.*, *103*, 17,919–17,932.

Iwata, T., H. Sekiguchi, Y. Matsumoto, H. Miyake, and K. Irikura (2000), Source process of the 2000 western Tottori Prefecture earthquake and near-source strong ground motions, paper presented at 2000 Fall Meeting, Seismol. Soc. of Jpn., Tokyo.

Ji, C., D. J. Wald, and D. V. Helmberger (2002), Source description of the 1999 Hector Mine California earthquake, part II: Complexity of slip history, *Bull. Seismol. Soc. Am.*, *92*, 1208–1226.

Johnson, K. M., Y. J. Hsu, P. Segall, and S. B. Yu (2001), Fault geometry and slip distribution of the 1999 Chi-Chi, Taiwan earthquake images from inversion of GPS data, *Geophys. Res. Lett.*, *28*, 2285–2288.

Jonsson, S., H. Zebker, P. Segall, and F. Amelung (2002), Fault slip distribution of the 1999 M_w 7.1 Hector Mine California earthquake estimated from satellite radar and GPS measurements, *Bull. Seismol. Soc. Am.*, *92*, 1377–1389.

Kame, N., and T. Yamashita (1999), A new light on arresting mechanism of dynamic earthquake faulting, *Geophys. Res. Lett.*, *26*, 1997–2000.

Kaverina, A., D. Dreger, and E. Price (2002), The combined inversion of seismic and geodetic data for the source process of the 16 October 1999 M_w 7.1 Hector Mine California earthquake, *Bull. Seismol. Soc. Am.*, *92*, 1266–1280.

Kikuchi, M., and Y. Fukao (1985), Iterative deconvolution of complex body waves from great earthquakes: The Tokachi-Oki earthquake of 1968, *Phys. Earth Planet. Inter.*, *37*, 235–248.

King, G. C. P. (1983), The accommodation of strain in the upper lithosphere of the Earth by self-similar fault systems; the geometrical origin of *b*-value, *Pure Appl. Geophys.*, *121*, 761–815.

King, G. C. P. (1986), Speculations on the geometry of the initiation and termination processes of earthquake rupture and its relation to morphology and geological structure, *Pure Appl. Geophys.*, *124*, 567–583.

King, G. C. P., and J. Nabelek (1985), The role of bends in faults in the initiation and termination of earthquake rupture, *Science*, *228*, 984–987.

King, G., and G. Yielding (1984), The evolution of a thrust fault system: Processes of rupture initiation, propagation and termination in the 1980 El Asnam (Algeria) earthquake, *Geophys. J. R. Astron. Soc.*, *77*, 915–933.

Larsen, S., R. Reilinger, H. Neugebauer, and W. Strange (1992), Global positioning system measurements of deformations associated with the 1987 Superstition Hills earthquake: Evidence for conjugate faulting, *J. Geophys. Res.*, *97*, 4885–4902.

Lay, T., and H. Kanamori (1981), An asperity model of great earthquake sequences, in *Earthquake Prediction: An International Review*, *Maurice Ewing Ser.*, vol. 4, edited by D. Simpson and P. Richards, pp. 579–592, AGU, Washington, D. C.

Lettis, W., J. Bachhuber, R. Witter, C. Brankman, C. E. Randolph, A. Barka, W. D. Page, and A. Kaya (2002), Influence of releasing step-overs on surface fault rupture and fault segmentation: Examples from the 17 August 1999 Izmit earthquake on the north Anatolian fault, Turkey, *Bull. Seismol. Soc. Am.*, *92*, 19–42.

Lin, A. M., et al. (2002), Co-seismic strike-slip and rupture length produced by the 2001 M_s 8.1 Central Kunlun earthquake, *Science*, *296*, 015–017.

Liu, H., and D. V. Helmberger (1983), The near-source ground motion of the 6 August 1979 Coyote Lake California earthquake, *Bull. Seismol. Soc. Am.*, *73*, 201–218.

Ma, K. F., J. Mori, S. J. Lee, and S. B. Yu (2001), Spatial and temporal distribution of slip for the 1999 Chi-Chi Taiwan earthquake, *Bull. Seismol. Soc. Am.*, *91*, 1069–1087.

Machette, M. N., S. F. Personius, A. R. Nelson, D. P. Schwartz, and W. R. Lund (1991), The Wasatch fault zone, Utah: Segmentation and history of Holocene earthquakes, *J. Struct. Geol.*, *13*, 137–149.

Madariaga, R. (1979), On the relation between seismic moment and stress drop in the presence of stress and strength heterogeneity, *J. Geophys. Res.*, *84*, 2243–2250.

Mai, P. M., and G. C. Beroza (2000), Source scaling properties from Finite-fault rupture models, *Bull. Seismol. Soc. Am.*, *90*, 604–615.

Mai, P. M., and G. C. Beroza (2002), A spatial random field model to characterize complexity in earthquake slip, *J. Geophys. Res.*, *107*(B11), 2308, doi:10.1029/2001JB000588.

Mai, P. M., P. Spudich, and Boatwright (2005), Hypocenter locations in finite-source rupture models, *Bull. Seismol. Soc. Am.*, in press.

Manighetti, I., G. C. P. King, Y. Gaudemer, C. Scholz, and C. Doubre (2001), Slip accumulation and lateral propagation of active normal faults in Afar, *J. Geophys. Res.*, *106*, 13,667–13,696.

Manighetti, I., G. King, and C. Sammis (2004), The role of off-fault damage in the evolution of normal faults, *Earth Planet. Sci. Lett.*, *217*, 399–408.

McGarr, A., and J. B. Fletcher (2002), Mapping apparent stress and energy radiation over fault zones of major earthquakes, *Bull. Seismol. Soc. Am.*, *92*, 1633–1646.

McGill, S. F., and C. M. Rubin (1999), Surficial slip distribution on the central Emerson fault during the June 28 1992 Landers earthquake, California, *J. Geophys. Res.*, *104*, 4811–4833.

McGuire, J. J., D. A. Wiens, P. J. Shore, and M. G. Bevis (1997), The March 9, 1994 (M_w 7.6) deep Tonga earthquake: Rupture outside the seismically active slab, *J. Geophys. Res.*, *102*, 15,163–15,182.

McGuire, J. J., L. Zhao, and T. H. Jordan (2002), Predominance of unilateral rupture for a global catalog of large earthquakes, *Bull. Seismol. Soc. Am.*, *92*, 3309–3317.

Mendoza, C. (1993), Coseismic slip of two large Mexican earthquakes from teleseismic body waveforms: Implications for asperity interaction in the Michoacan plate boundary segment, *J. Geophys. Res.*, *98*, 8197–8210.

Mendoza, C. (1995), Finite-fault analysis of the 1979 March 14 Petatlan, Mexico, earthquake using teleseismic P waveforms, *Geophys. J. Int.*, *121*, 675–683.

Mendoza, C., and E. Fukuyama (1996), The July 12, 1993, Hokkaido-Nansei-Oki, Japan earthquake: Coseismic slip pattern from strong-motion and teleseismic recordings, *J. Geophys. Res.*, *101*, 791–801.

Mendoza, C., and S. H. Hartzell (1988), Inversion for slip distribution using teleseismic P waveforms: North Palm Springs, Borah Peak, and Michoacan earthquakes, *Bull. Seismol. Soc. Am.*, *78*, 1092–1111.

Mendoza, C., and S. Hartzell (1999), Fault slip distribution of the 1995 Colima-Jalisco, Mexico earthquake, *Bull. Seismol. Soc. Am.*, *89*, 1338–1344.

Mendoza, C., S. Hartzell, and T. Monfret (1994), Wide-band analysis of the 3 March 1985 central Chile earthquake: Overall source process and rupture history, *Bull. Seismol. Soc. Am.*, *84*, 269–283.

Michel, R., and J. Avouac (2002), Deformation due to the 17 August 1999 Izmit, Turkey, earthquake measured from SPOT images, *J. Geophys. Res.*, *107*(B4), 2062, doi:10.1029/2000JB000102.

Mikumo, T., and T. Miyatake (1978), Dynamic rupture process on a three dimensional fault with non-uniform friction and near-field waves, *Geophys. J. R. Astron. Soc.*, *54*, 417–438.

Miller, S. A. (2002), Properties of large ruptures and the dynamical influence of fluids on earthquakes and faulting, *J. Geophys. Res.*, *107*(B9), 2182, doi:10.1029/2000JB000032.

Mori, J. (1996), Rupture directivity and slip distribution of the *M* 4.3 foreshock to the 1992 Joshua Tree earthquake, southern California, *Bull. Seismol. Soc. Am.*, *86*, 805–810.

Nielsen, S. B., and K. Olsen (2000), Constraints on stress and friction from dynamic rupture models of the 1994 Northridge California earthquake, *Pure Appl. Geophys.*, *157*, 2029–2046.

Oglesby, D. D., and R. J. Archuleta (1997), A faulting model for the 1992 Petrolia earthquake: Can extreme ground acceleration be a source effect?, *J. Geophys. Res.*, *102*, 1877–1897.

Oglesby, D. D., and S. M. Day (2001), Fault geometry and the dynamics of the 1999 Chi-Chi (Taiwan) earthquake, *Bull. Seismol. Soc. Am.*, *91*, 1099–1111.

Papageorgiou, A. S. (2003), The barrier model and strong ground motion, *Pure Appl. Geophys.*, *160*, 603–634.

Peacock, D. C. P. (2002), Propagation, interaction and linkage in normal fault systems, *Earth Sci. Rev.*, *58*, 121–142.

Peacock, D. C. P., and D. J. Sanderson (1996), Effects of propagation rate on displacement variations along faults, *J. Struct. Geol.*, *18*, 311–320.

Pegler, G., and S. Das (1996), Analysis of the relationship between seismic moment and fault length for large crustal strike-slip earthquakes between 1977–92, *Geophys. Res. Lett.*, *23*, 905–908.

Peltzer, G., K. W. Hudnut, and K. L. Feigl (1994), Analysis of coseismic surface displacement gradients using radar interferometry: New insights into the Landers earthquake, *J. Geophys. Res.*, *99*, 21,971–21,981.

Peltzer, G., F. Crampé, and G. King (1999), Evidence of nonlinear elasticity of the crust from the M_w 7.6 Manyi (Tibet) earthquake, *Science*, *286*, 272–275.

Perfettini, H., R. S. Stein, R. Simpson, and M. Cocco (1999), Stress transfer by the 1988–1989 *M* = 5.3 and 5.4 Lake Elsman foreshocks to the Loma Prieta fault: Unclamping at the site of peak mainshock slip, *J. Geophys. Res.*, *104*, 20,169–20,182.

Poliakov, A. N. B., R. Dmowska, and J. R. Rice (2002), Dynamic shear rupture interactions with fault bends and off-axis secondary faulting, *J. Geophys. Res.*, *107*(B11), 2295, doi:10.1029/2001JB000572.

Rice, J. R. (1980), The mechanics of earthquake rupture, in *Physics of the Earth's Interior*, edited by A. Dziewonski and E. Boschi, pp. 555–649, Elsevier, New York.

Romanowicz, B. (1992), Strike-slip earthquakes on quasi-vertical transcurrent faults: Inferences for general scaling relations, *Geophys. Res. Lett.*, *19*, 481–484.

Roumelioti, Z., D. Dreger, A. Kiratzi, and N. Theodoulidis (2003), Slip distribution of the 7 September 1999 Athens earthquake inferred from an empirical Green's function study, *Bull. Seismol. Soc. Am.*, *93*, 775–782.

Ruff, L. J., and A. D. Miller (1994), Rupture process of large earthquakes in the northern Mexico subduction zone, *Pure Appl. Geophys.*, *142*, 101–149.

Salichon, J., B. Delouis, P. Lundgren, D. Giardini, M. Costantini, and P. Rosen (2003), Joint inversion of broadband teleseismic and interferometric synthetic aperture radar (InSAR) data for the slip history of the M_w = 7.7, Nazca ridge (Peru) earthquake of 12 November 1996, *J. Geophys. Res.*, *108*(B2), 2085, doi:10.1029/2001JB000913.

Scholz, C. H. (1982), Scaling laws for large earthquakes: Consequences for physical models, *Bull. Seismol. Soc. Am.*, *72*, 1–14.

Scholz, C. H. (1990), *The Mechanics of Earthquakes and Faulting*, 1st ed., Cambridge Univ. Press, New York.

Scholz, C. H. (1994a), A reappraisal of large earthquake scaling, *Bull. Seismol. Soc. Am.*, *84*, 215–218.

Scholz, C. H. (1994b), Reply to comments on "A reappraisal of large earthquake scaling," *Bull. Seismol. Soc. Am.*, *84*, 1677–1678.

Scholz, C. H. (2000), Evidence for a strong San Andreas fault, *Geology*, *28*, 163–166.

Scholz, C. H. (2002), *The Mechanics of Earthquakes and Faulting*, 2nd ed., 471 pp., Cambridge Univ. Press, New York.

Schwartz, D. P., and K. J. Coppersmith (1984), Fault behavior and characteristic earthquakes: Examples from the Wasatch and San Andreas faults, *J. Geophys. Res.*, *89*, 5681–5698.

Segall, P., and D. D. Pollard (1980), Mechanics of discontinuous faults, *J. Geophys. Res.*, *85*, 4337–4350.

Sekiguchi, H., and T. Iwata (2002), Rupture process of the 1999 Kocaeli Turkey earthquake estimated from strong-motion waveforms, *Bull. Seismol. Soc. Am.*, *92*, 300–311.

Sekiguchi, H., K. Irikura, T. Iwata, Y. Kakehi, and M. Hoshiba (1996), Determination of the location of faulting beneath Kobe during the 1995 Hyogo-ken Nanbu Japan earthquake from near-source particle motion, *Geophys. Res. Lett.*, *23*, 387–390.

Sharp, R. V. (1982), Comparison of 1979 surface faulting with earlier displacements in the Imperial Valley, in *The Imperial Valley, California, Earthquake of October 15, 1979*, *U.S. Geol. Surv. Prof. Pap.*, *1254*, 213–221.

Sharp, R. V., et al. (1989), Surface faulting along the Superstition Hills fault zone and nearby faults associated with the earthquakes of 24 November 1987, *Bull. Seismol Soc. Am.*, *79*, 252–281.

Shaw, B. E., and C. H. Scholz (2001), Slip-length scaling in large earthquakes: Observations and theory and implications for earthquake physics, *Geophys. Res. Lett.*, *28*, 2991–2994.

Shaw, J. H., A. Plesch, J. F. Dolan, T. L. Pratt, and P. Fiore (2002), Puente Hills blind-thrust system, Los Angeles, California, *Bull. Seism. Soc. Am.*, *92*, 2946–2960.

Sibson, R. H. (1984), Roughness at the base of the seismogenic zone: Contributing factors, *J. Geophys. Res.*, *89*, 5791–5799.

Sibson, R. H. (1985), Stopping of earthquake ruptures at dilatational fault jogs, *Nature*, *316*, 248–251.

Sibson, R. H. (1986), Earthquakes and rock deformation in crustal fault zones, *Annu. Rev. Earth Planet. Sci.*, *14*, 149–175.

Sibson, R. H. (1989), Earthquake faulting as a structural process, *J. Struct. Geol.*, *11*, 1–14.

Sieh, K. (1996), The repetition of large earthquake ruptures, *Proc. Natl. Acad. Sci. U.S.A.*, *93*, 3764–3771.

Sieh, K., et al. (1993), Near-field investigations of the Landers earthquake sequence, April to July 1992, *Science*, *260*, 171–176.

Somerville, P., K. Irikura, R. Graves, S. Sawada, D. Wald, N. Abrahamson, Y. Iwasaki, T. Kagawa, N. Smith, and A. Kowada (1999), Characterizing crustal earthquake slip models for the prediction of strong ground motion, *Seismol. Res. Lett.*, *70*(1), 59–80.

Spence, W., C. Mendoza, E. R. Engdahl, G. L. Choy, and E. Norabuena (1999), Seismic subduction of the Nazca ridge as shown by the 1996–97 Peru earthquakes, *Pure Appl. Geophys.*, *154*, 753–776.

Steidl, J. H., R. J. Archuleta, and S. H. Hartzell (1991), Rupture history of the 1989 Loma Prieta California earthquake, *Bull. Seismol. Soc. Am.*, *81*, 1573–1602.

Stein, R. S., and W. Thatcher (1981), Seismic and aseismic deformation associated with the 1952 Kern County, California, earthquake and relationship to the Quaternary history of the White Wolf fault, *J. Geophys. Res.*, *86*, 4913–4928.

Susong, D. D., S. U. Janecke, and R. L. Bruhn (1990), Structure of a fault segment boundary in the Lost River fault zone, Idaho, and possible effect on the 1983 Borah Peak earthquake rupture, *Bull. Seismol. Soc. Am.*, *80*, 57–68.

Takeo, M. (1988), Rupture process of the 1980 Izu-Hanto-Toho-Oki earthquake deduced from strong motion seismograms, *Bull. Seismol. Soc. Am.*, *78*, 1074–1091.

Takeo, M. (1990), Fault heterogeneity of inland earthquakes in Japan, *Bull. Earthquake Res. Inst. Univ. Tokyo*, *65*(2), 541–569.

Takeo, M., and N. Mikami (1987), Inversion of strong motion seismograms for the source process of the Naganoken-Seibu earthquake of 1984, *Tectonophysics*, *144*, 271–285.

Tanioka, Y., L. Ruff, and K. Satake (1996), The Sanriku-Oki Japan earthquake of December 28 1994 (M_w 7.7), Rupture of a different asperity from a previous earthquake, *Geophys. Res. Lett.*, *23*, 1465–1468.

Tapponnier, P., F. J. Ryerson, J. Van der Woerd, A.-S. Mériaux, and C. Lasserre (2001), Long-term slip rates and characteristic slip: Keys to active fault behaviour and earthquake hazard, *C. R. Acad. Sci., Ser. IIa Sci. Terre Planetes*, *333*, 483–494.

Tchalenko, J. S., and M. Berberian (1975), Dasht-e Bayaz fault, Iran: Earthquake and earlier related structures in bed rock, *Geol. Soc. Am. Bull.*, *86*, 703–709.

Thatcher, W. (1990), Order and diversity in the modes of circum-Pacific earthquake recurrence, *J. Geophys. Res.*, *95*, 2609–2623.

Thatcher, W., G. Marshall, and M. Lisowski (1997), Resolution of fault slip along the 470-km-long rupture of the great 1906 San Francisco earthquake and its implications, *J. Geophys. Res.*, *102*, 5353–5367.

Velasco, A. A., C. J. Ammon, T. Lay, and M. Hagerty (1996), Rupture process of the 1990 Luzon, Philippines (M_w 7.7) earthquake, *J. Geophys. Res.*, *101*, 2419–2434.

Wald, D. (1992), Strong motion and broadband teleseismic analysis of the 1991 Sierra Madre, California, earthquake, *J. Geophys. Res.*, *97*, 11,033–11,046.

Wald, D. J. (1996), A dislocation model of the 1995 Kobe Japan earthquake determined from strong motion, teleseismic and geodetic data, *J. Phys. Earth*, *44*, 489–503.

Wald, D. J., and T. H. Heaton (1994), Spatial and temporal distribution of slip for the 1992 Landers California earthquake, *Bull. Seismol. Soc. Am.*, *84*, 668–691.

Wald, D. J., and P. G. Somerville (1995), Variable slip rupture model of the great 1923 Kanto Japan earthquake: Geodetic and body-waveform analysis, *Bull. Seismol. Soc. Am.*, *85*, 159–177.

Wald, D. J., D. V. Helmberger, and S. H. Hartzell (1990), Rupture process of the 1987 Superstition Hills earthquake from the inversion of strong-motion data, *Bull. Seismol. Soc. Am.*, *80*, 1079–1098.

Wald, D. J., H. Kanamori, D. V. Helmberger, and T. H. Heaton (1991), Rupture model of the 1989 Loma Prieta earthquake from the inversion of strong-motion and broadband teleseismic data, *Bull. Seismol. Soc. Am.*, *81*, 1540–1572.

Wald, D. J., T. H. Heaton, and K. W. Hudnut (1996), The slip history of the 1994 Northridge California earthquake determined from strong motion, teleseismic, GPS and leveling data, *Bull. Seismol. Soc. Am.*, *86*, 49–70.

Walker, G. (1999), Volcanic rift zones and their intrusion swarms, *J. Volcanol. Geotherm. Res.*, *94*, 21–34.

Walsh, J. J., and J. Watterson (1987), Distribution of cumulative displacement and of seismic slip on a single normal fault surface, *J. Struct. Geol.*, *9*, 1039–1046.

Walsh, J. J., and J. Watterson (1988), Analysis of the relationship between displacements and dimensions of faults, *J. Struct. Geol.*, *10*, 238–347.

Ward, S. N. (1997), Dogtails versus rainbows: Synthetic earthquake rupture models as an aid in interpreting geological data, *Bull. Seismol. Soc. Am.*, *87*, 1422–1441.

Wells, D. L., and K. J. Coppersmith (1994), New empirical relationships among magnitude, rupture length, rupture width, rupture area, and surface displacement, *Bull. Seismol. Soc. Am.*, *84*, 974–1002.

Wesnousky, S. G. (1988), Seismological and structural evolution of strike-slip faults, *Nature*, *335*, 340–342.

Wesnousky, S. G. (1994), The Gutenberg-Richter or characteristic earthquake distribution, which is it?, *Bull. Seismol. Soc. Am.*, *84*, 1940–1959.

Willemse, E. J. M. (1997), Segmented normal faults: Correspondence between three dimensional mechanical models and field data, *J. Geophys. Res.*, *102*, 675–692.

Wu, C., M. Takeo, and S. Ide (2001), Source process of the Chi-Chi earthquake: A joint inversion of strong motion data and global positioning system data with a multifault model, *Bull. Seismol. Soc. Am.*, *91*, 1128–1143.

Yagi, Y., and M. Kikuchi (2000), Source rupture process of the Kocaeli Turkey earthquake of August 17 1999, obtained by joint inversion of near-field data and teleseismic data, *Geophys. Res. Lett.*, *27*, 1969–1972.

Yagi, Y., M. Kikuchi, and S. Yoshida (1999), Comparison of the coseismic rupture with the aftershock distribution in the Hyuga-Nada earthquakes of 1996, *Geophys. Res. Lett.*, *26*, 3161–3164.

Yoshida, S., K. Koketsu, B. Shibazaki, T. Sagiya, T. Kato, and Y. Yoshida (1996), Joint inversion of near- and far-field waveforms and geodetic data for the rupture process of the 1995 Kobe earthquake, *J. Phys. Earth*, *44*(5), 437–454.

Zachariasen, J., and K. Sieh (1995), The transfer of slip between two en echelon strike-slip faults: A case study from the 1992 Landers earthquake, southern California, *J. Geophys. Res.*, *100*, 15,281–15,301.

Zeng, Y. H., and J. G. Anderson (1996), A composite source model of the 1994 Northridge earthquake using genetic algorithms, *Bull. Seismol. Soc. Am.*, *86*, S71–S83.

Zeng, Y. H., and J. G. Anderson (2000), Evaluation of numerical procedures for simulating near-fault long-period ground motions using Zeng's method, *Rep. 2000/01*, Pac. Earthquake Eng. Res. Cent., Berkeley, Calif.

Zhang, P., F. Mao, and D. B. Slemmons (1999), Rupture terminations and size of segment boundaries from historical earthquake ruptures in the Basin and Range Province, *Tectonophysics*, *308*, 37–52.

Zhang, W., T. Iwata, K. Irikura, H. Sekiguchi, and M. Bouchon (2003), Heterogeneous distribution of the dynamic source parameters of the 1999 Chi-Chi, Taiwan, earthquake, *J. Geophys. Res.*, *108*(B5), 2232, doi:10.1029/2002JB001889.

Zobin, V. M., and V. I. Levina (1998), Rupture history of the January 1 1996 M_s 6.6 volcanic earthquake preceding the simultaneous eruption of Karymsky and Akademia Nauk volcanoes in Kamchatka, Russia, *J. Geophys. Res.*, *103*, 18,315–18,324.

Zobin, V. M., and V. I. Levina (2001), The rupture process of the M_w 7.8 Cape Kronotsky, Kamchatka, earthquake of 5 December 1997 and its relationship to foreshocks and aftershocks, *Bull. Seismol. Soc. Am.*, *91*, 1619–1628.

M. Campillo and I. Manighetti, Laboratoire de Géophysique Interne et Tectonophysique de Grenoble, BP 53, F-38041 Grenoble, France. (imanighe@obs.ujf-grenoble.fr)

G. King, Laboratoire de Tectonique, Institut de Physique du Globe de Paris, 4 Place Jussieu, F-75252 Paris, France.

P. M. Mai, Institute of Geophysics, ETH-Zurich, CH-8093 Zurich, Switzerland.

C. Sammis, Department of Earth Sciences, University of Southern California, Los Angeles, CA 90089-0740, USA.

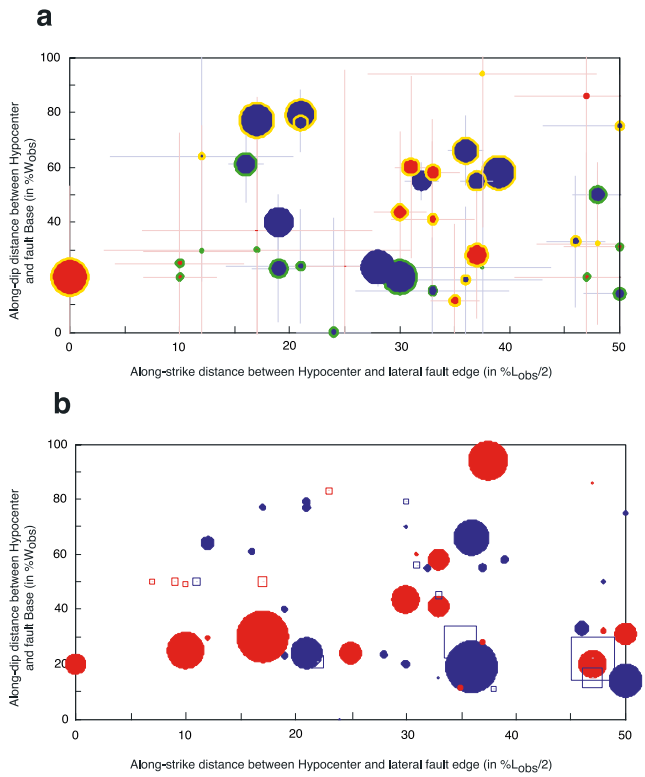

Figure 11. Distribution of hypocenters with respect to fault plane edges. X axis is along-strike position (in percent of L_{obs}) of hypocenters with respect to lateral fault plane edges (irrespective of which side). Y axis is along-dip position (in percent W_{obs}) of hypocenters with respect to fault plane base. Dip-slip and strike-slip faults are in blue and red, respectively. (a) Symbol size proportional to magnitude. Data are from Table 2 (averaged per earthquake; in few cases, best model is preferred). Uncertainties on hypocenter positions are assigned to 5 km in both x and y. Yellow and green circled symbols are for slip profiles tapering downward and upward, respectively. (b) Symbol size proportional to D_{max}/L_{model}. Data are from Tables 2 (solid symbols) and 3 (open symbols).

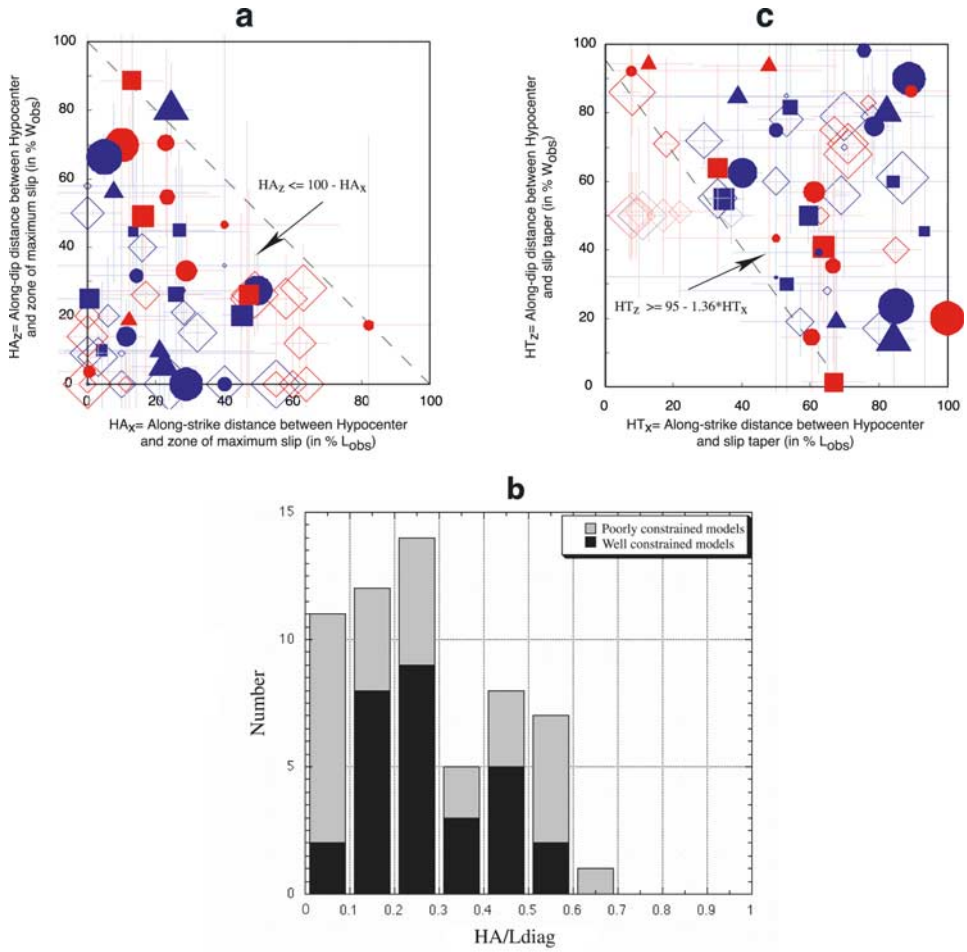

Figure 12. Position of hypocenters (H) with respect to zone of maximum slip (major asperity, A) and to slip taper (T) for earthquake faults with triangular slip profiles (both along strike and dip). Colors and uncertainties are as in Figure 11. Solid symbols are for best constrained models (from Table 2, as in Figure 11); open symbols are for poorly constrained models (from Table 3). Symbol shape indicates degree of asymmetry of along-strike slip profiles. For ruptures wider than 40 km, however, asymmetry is that of along-dip slip profiles. For models with tabular data, distances HA are those between hypocenter and apex of best fitting triangle. For models with no tabular data, distances HA and HT are estimated from visual inspection of the models (when hypocenters lie close to their zone of maximum slip, HA is fixed to zero; open symbols falling on any of the axes are therefore not well constrained). In all plots, symbol size is proportional to magnitude. (a) Position of hypocenter with respect to zone of maximum slip, with distances in percent of L_{obs} and W_{obs}. (b) Histogram of HA ($HA = (Ha_x^2 + Ha_z^2)^{0.5}$, all in km) normalized by diagonal length ($L_{diag} = (L^2 + W^2)^{0.5}$, all in km) of events. (c) Position of hypocenter with respect to slip taper, with distances in percent of L_{obs} and W_{obs}.

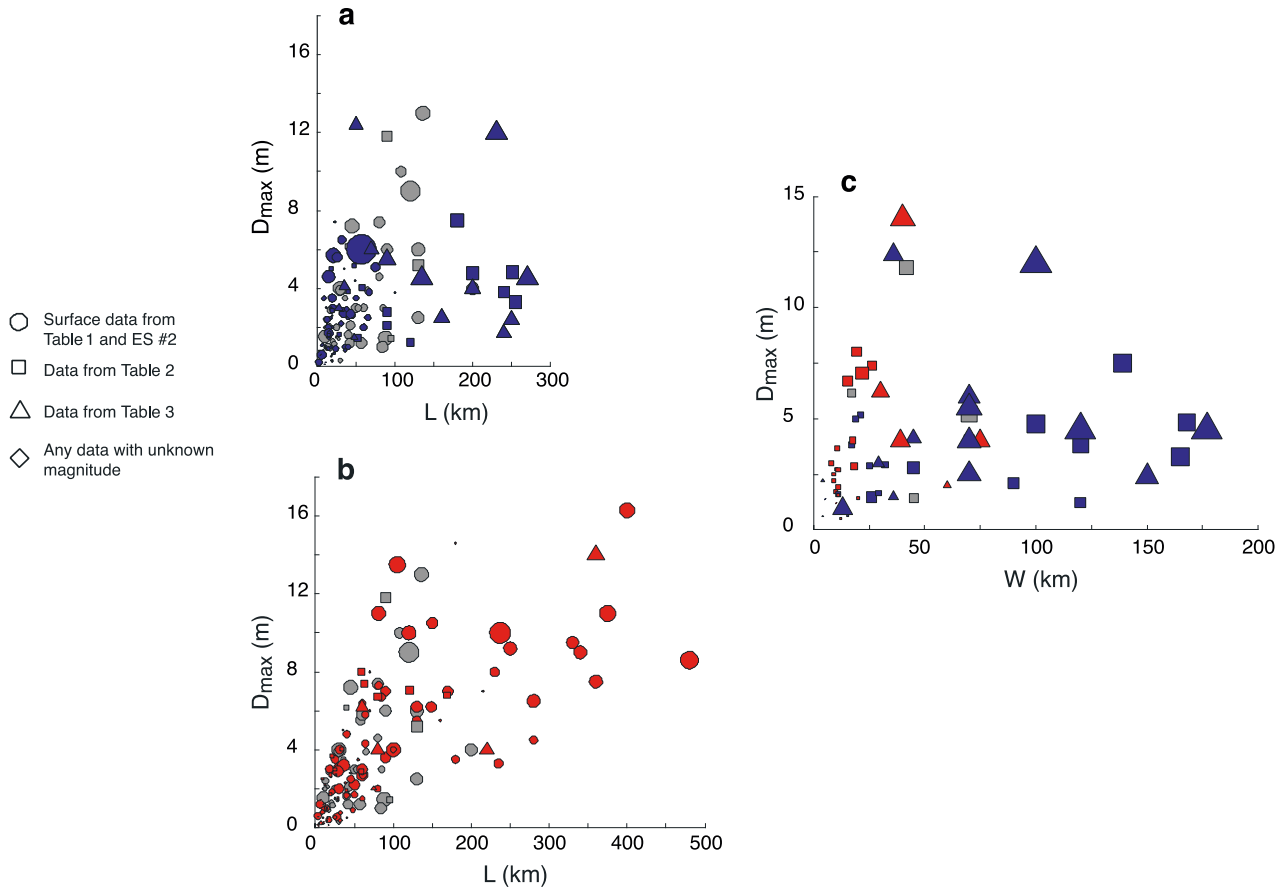

Figure 13. Scaling relations for the earthquakes analyzed. (a) Maximum displacement (D_{max}) versus length (L) for dip-slip (blue) and oblique (gray) faults (from Tables 1, 2, and 3 and ES02). (b) Maximum displacement (D_{max}) versus length (L) for strike-slip (red) and oblique (gray) faults (from Tables 1, 2, and 3 and ES02). (c) Maximum displacement (D_{max}) versus width (W) for dip-slip (blue), strike-slip (red), and oblique (gray) faults (from Tables 2 and 3). Symbol size is proportional to magnitude. Where that is unknown (as for earthquake sequences), symbol size is set to an arbitrary value (corresponding to M = 6). L is L_{obs} for data from Table 1, L_{meas} is for data from ES022, and L_{model} id for data from Tables 2 and 3 (same for W).